SPAWAR
Systems Center
PACIFIC

TECHNICAL REPORT 2085
August 2016

FANS Simulation of Propeller Wash at Navy Harbors (ESTEP Project ER-201031)

Pei-Fang Wang
SSC Pacific

Hamn-Ching Chen
Texas A&M University

SSC Pacific
San Diego, CA 92152-5001

SSC Pacific
San Diego, California 92152-5001

K. J. Rothenhaus, CAPT, USN
Commanding Officer

C. A. Keeney
Executive Director

ADMINISTRATIVE INFORMATION

This report was was developed in support of Environmental Security Technology Certification Program (ESTEP) Project ER-201-031 by the Environmental Sciences Branch (Code 71750), of the Advanced Systems and Applied Sciences Division (Code 71700), Space and Naval Warfare Systems Center Pacific (SSC Pacific), San Diego, CA; and the Ocean Engineering Program, Zachry Department of Civil Engineering, Texas A&M University, College Station, TX,

Released by
P. J. Earley, Head
Environmental Sciences Branch

Under authority of
A. J. Ramirez, Head
Advanced Systems & Applied Sciences Division

SB

EXECUTIVE SUMMARY

Propeller wash induces high shear stresses on seafloor which may cause sediment resuspension in Department of Defense (DoD) harbors. To improve understanding of the sediment erosion, transport, dispersion, and re-deposition processes, it is desirable that advanced computational fluid dynamics models should be used to provide detailed resolution of the velocities and bottom shear stresses induced by the propeller wash in confined shallow water basins. In this study, the Finite-Analytic Navier–Stokes code was employed to solve the Reynolds-Averaged Navier–Stokes equations in conjunction with advanced near-wall turbulence model for several propeller-wash scenarios involving an Arleigh Burke-class destroyer with twin-screw propellers and a tugboat with two ducted propellers. This model enables us to evaluate the effect of water depth, ship speed, propeller rotating speed, and pier wall configuration on the propeller-induced shear stresses distributions.

CONTENTS

EXECUTIVE SUMMARY ..... **iii**

1. INTRODUCTION **1**

2. SIMULATION SCENARIOS FOR DDG 51 SHIP **4**

2.1 FANS Model Simulation Results for DDG 51 Ship 5
2.2 Disturbed Velocity Profiles 6
2.3 Estimated Bottom Shear Stresses 12

3. SIMULATION SCENARIOS FOR TUGBOAT WITH DUCTED PROPELLERS **15**

3.1 FANS Model Simulation Results for Tugboat with Ducted Propellers 18
3.2 Disturbed Velocity Profiles 19
3.3 Estimated Bottom Shear Stresses 29

REFERENCES **33**

Figures

1. DDG 51 ship and P4876 propeller geometry 4
2. Computational domain and numerical grids 5
3. Longitudinal velocity contours and velocity vectors near seabed 7
4. Velocity profiles at the keel plane 8
5. Axial velocity contours and velocity vector plots around the propeller 8
6. Propeller-induced flow field at selected stations 9
7. Propeller-induced swirling flows 11
8. Shear stress distribution on the seabed 12
9. Surface plots of shear stresses on the seabed 13
10. Surface plots of seabed shear stresses around the twin-screw propellers 14
11. Tugboat and ducted propeller geometry 15
12. Harbor configurations for tugboat propeller wash simulations 17
13. Computational domain and numerical grids 18
14. Axial velocity contours on the vertical propeller center plane at t/T_o = 100, 200, 300, 400, and 500 (T_o = 0.3 s); Case 1 with propeller blowing to open water 20
15. Axial velocity contours on the horizontal propeller center plane (left) and free surface (right) at t/T_o = 100, 300, and 500 (T_o = 0.3 sec); Case 1 with propeller blowing to open water 21
16. Axial velocity contours on the vertical propeller center plane at t/T_o = 100, 132, 200, 300, 400, and 500 (To = 0.3 sec); Case 2 with propeller blowing toward pier wall 22
17. Axial velocity contours on the horizontal propeller center plane (left) and free surface (right) at t/T_o = 100, 300, and 500 (T_o = 0.3 sec); Case 2 with propeller blowing toward pier wall. 23
18. Pressure contours on pier wall and sea bottom, t/T_o = 160 and 320; Case 2 with propeller blowing toward a pier wall 24
19. Axial velocity contours behind the right propeller (near pier wall); Case 3 with propeller blowing parallel to pier wall 25
20. Axial velocity contours behind the left propeller (away from pier wall); Case 3 with propeller blowing parallel to pier wall 25
21. Axial velocity contours on the horizontal propeller center plane (left) and free surface (right) at t/T_o = 100, 200, 300, 400, and 500; Case 3 with propeller blowing parallel to pier wall 26

22. Axial velocity contours at horizontal propeller center plane (top) and selected cross-sections (bottom); Case 3 with propeller blowing parallel to pier wall 27
23. Propeller-induced swirling flows (normalized by U_o) at $t/T_o = 500$ 28
24. Shear stress distribution on the seabed at t/T_o = 100, 200, 300, 400, 460, and 500; Case 1 with propeller blowing to open water 29
25. Shear Stress distribution on the seabed at t/T_o = 100, 200, 300, 400, 460, and 500; Case 2 with propeller blowing to pier wall 30
26. Shear Stress distribution on the seabed at t/T_o = 100, 200, 300, 400, 460, and 500; Case 3 with propeller blowing parallel to pier wall 31

Tables

1. Propeller information for DDG-51 ship in FANS simulation 4
2. Maximum shear stresses in different regions of the seabed 14
3. Propeller information for tugboat in FANS simulation 16

1. INTRODUCTION

In this study, the Finite-Analytic Navier–Stokes (FANS) code was employed for propeller-wash study in U.S. Navy harbors. The FANS code solves Reynolds-Averaged Navier–Stokes (RANS) equations together with advanced turbulence models in general curvilinear coordinate systems using overset (chimera) grids. The overset grid system facilitated the simulation of arbitrary relative motions among various computational grid blocks such as those encountered wave-current-body interactions and vortex-induced vibrations. The FANS code consists of the following main components: (1) finite-analytic method for the solution of compressible and incompressible RANS equations and energy equation in general curvilinear coordinates; (2) dynamic chimera domain decomposition technique for overlapped, embedded, or matched grids including relative motions; (3) near-wall Reynolds stress (second-moment) and two-layer k-ε turbulence models for turbulent boundary layer and wake flows; (4) large eddy simulation for unsteady chaotic eddy motions, (5) linear and nonlinear wave effects; (6) level-set method for interface-capturing between two different fluids; (7) detailed propeller flow simulations or interactive coupling with propeller performance programs; (8) coupling with six-degree-of-freedom motion program for ship, structure, wave, and current interactions; and (9) multi-processor parallelization for large-scale computational fluid dynamics (CFD) applications. The combination of these methods provides a unique capability for modeling complex fluid flow and heat transfer around practical three-dimensional configurations including viscous and violent free surface effects.

The FANS code has been used extensively for the simulation of ship motions under very shallow water conditions. Chen and Chen (1998) and Chen, Liu, Huang, and Davis (2000) performed berthing simulations for DDG-51 and AOE-6 ships with underkeel clearance ranging from 5 to 20% of the ship draft. Chen and Huang (2003) and Huang and Chen (2003) also performed time-domain simulation of berthing operations involving a modular hybrid pier (MHP) with 2 mooring dophins, 2 moored LHD ships, one berthing LHD ship, a tug boat, 7 fenders and 12 mooring lines. In these simulations, a very shallow water depth of 28 ft was intentionally chosen to confine the underkeel clearance of the moored and docking ships to 1 ft or 3.7% of the ship draft (= 27 ft). The FANS code was also used in Chen, Lin and Huang (2002a, 2002b) and Chen, Lin, Liut and Huang (2003) for the study of multiple-ship interactions in dredged navigational channels. More recently, Huang and Chen (2007, 2010) used the FANS code for site-specific passing ship effects on a docked ship moored to a floating pier in Norfolk harbor. These simulation results clearly demonstrated the capability of the FANS code to model complex interactions between Navy harbor facilities and its client ships in a real waterfront ambience, including site-specific conditions such as sea bed bathymetry, shorelines, harbor geometry, navigation channels, hull shapes, and arbitrary ship motions.

In addition to the simulation of multiple-ship interactions, the FANS code was also used extensively for a wide range of fluid-structure interaction problems, including propeller-ship interactions (Chen and Lee, 2004; Lee and Chen, 2005; Pontaza, Chen and Lee, 2006), greenwater and extreme slamming of ship in random waves (Chen and Chen, 2014), wet-deck slamming (Chen and Yu, 2009), LNG tank sloshing (Chen, 2011), hurricane wave loads on offshore platform and jack-up structure (Chen, 2010, 2013), vortex-induced vibration of deep water risers (Huang, Chen and Chen, 2010, 2011, 2012) and riser interferences (Chen, Chen and Huang, 2013), and scour around bridges (Chen, 2002; Briaud, Chen, Li and Nurtjahyo, 2004; and Briaud and Chen, 2006).

In the FANS code, the unsteady Reynolds-Averaged Navier–Stokes (RANS) equations for incompressible flow in curvilinear coordinates are formulated in general curvilinear coordinates $(\xi^i, t) = (\xi, \eta, \varsigma, t)$:

$$U^i_{,i} = 0 \tag{1}$$

$$\frac{\partial U^i}{\partial t} + U^j U^i_{,j} + \left(\overline{u^i u^j}\right)_{,j} + g^{ij} p_{,j} - \frac{1}{Re} g^{jk} U^i_{,jk} = 0\,, \tag{2}$$

where U^i and u^i represent the mean and fluctuating velocity components, and g^{ij} is conjugate metric tensor. t is time, p is pressure, and $Re = U_o L/\nu$ is the Reynolds number based on a characteristic length L, a reference velocity U_o, and the kinematic viscosity ν. Equation (1) represents the continuity equation and Equation (2) represents the mean momentum equation. The equations are written in tensor notation with the usual summation convention assumed. The subscripts, $_{,j}$ and $_{,jk}$, represent the covariant derivatives.

In this study, the two-layer turbulence model of Chen and Patel (1988) is employed to provide closure for the Reynolds stress tensor $\overline{u^i u^j}$. In this approach, the Reynolds stresses are related to the corresponding mean rate of strain through an isotropic eddy viscosity ν_t:

$$-\overline{u^i u^j} = 2\nu_t S^{ij} - \frac{2}{3} g^{ij} k \tag{3}$$

$$\text{with } S^{ij} = \frac{1}{2}\left(g^{ik} U^j_{,k} + g^{jk} U^i_{,k}\right); \quad k = \frac{1}{2} g^{ij} \overline{u^i u^j}\,, \tag{4}$$

where S^{ij} represent the contravariant components of the rate-of-strain tensor and k is the turbulent kinetic energy. Substituting Equation (3) into Equation (2) yields

$$\frac{\partial U^i}{\partial t} + U^j U^i_{,j} + g^{ij}\left(p + \frac{2}{3}k\right)_{,j} - 2\nu_t S^{ij} - \frac{1}{R_t} g^{jk} U^i_{,jk} = 0\,. \tag{5}$$

The quantity $1/R_t = 1/\mathrm{Re} + \nu_t$ represents the effective viscosity. In the fully turbulent flow region away from the solid walls, the standard k-ε model is employed to solve the transport equations for turbulent kinetic energy k and its dissipation rate ε:

$$\frac{\partial k}{\partial t} + U^j k_{,j} - \left(\frac{1}{R_k} g^{ij} k_{,j}\right)_{,i} - G + \varepsilon = 0 \tag{6}$$

$$\frac{\partial \varepsilon}{\partial t} + U^j \varepsilon_{,j} - \left(\frac{1}{R_\varepsilon} g^{ij} \varepsilon_{,j}\right)_{,i} - C_{\varepsilon 1}\frac{\varepsilon}{k} G + C_{\varepsilon 2}\frac{\varepsilon^2}{k} = 0\,, \tag{7}$$

where the eddy viscosity ν_t and the production term G are given by

$$\nu_t = C_\mu \frac{k^2}{\varepsilon}\;; \quad G = 2\nu_t g_{im} g_{jn} S^{ij} S^{mn}\,. \tag{8}$$

The effective viscosities in Equations (6) and (7) are taken as $1/R_k = 1/\mathrm{Re} + \nu_t/\sigma_k$ and $1/R_\varepsilon = 1/\mathrm{Re} + \nu_t/\sigma_\varepsilon$, respectively.

In the current two-layer approach (Chen and Patel, 1988), the dissipation rate in the near wall region is determined from the turbulent kinetic energy and the dissipation length scale ℓ_ε to account for the wall effects:

$$\varepsilon = \frac{k^{3/2}}{\ell_\varepsilon} \; ; \quad \ell_\varepsilon = C_\ell y\left[1 - \exp(-R_y / A_\varepsilon)\right]. \tag{10}$$

Using this relationship, the turbulent kinetic energy can be determined from Equation (6) with the following eddy viscosity distribution:

$$\nu_t = C_\mu \sqrt{k}\ell_\mu; \quad \ell_\mu = C_\ell y\left[1 - \exp(-R_y / A_\mu)\right]. \tag{11}$$

The constants C_ℓ, A_μ and A_ε are given in Chen and Patel (1988) are chosen to yield a smooth distribution of eddy viscosity between the two regions.

The above equations are solved numerically using the finite-analytic method developed by Chen and Chen (1984), Chen, Patel and Ju (1990), Chen, Bravo, Chen and Xu (1995), and Pontaza, Chen and Reddy (2005). A detailed description of the finite-analytic method is provided in Space and Naval Warfare Systems Center Pacific (SSC Pacific) Technical Report 3293, FANS-3D Users Guide Chen and Wang, 2016).

2. SIMULATION SCENARIOS FOR DDG 51 SHIP

FANS simulations were performed for a USS Arleigh Burke (DDG 51) ship as shown in Figure 1 under two different water depths (10.0588 and 11.5824 m) and two different propeller rotating speeds (26 and 51 rpms). The length of the DDG 51 ship is 142.04 m (466 ft) and the designed draft is 9.4488 m. The diameter of the twin-screw propellers is 5.4864 m (18 ft), and the center of propeller axis is located at 5.7912 m below the mean water level. For the shallow water case with 10.0584 m (33 ft) water depth, the underkeel clearance is only 0.6096 m (2 ft) beneath the sonar dome and the minimum gap between the propeller tip and the sea bottom is 1.524 m (5 ft). The propeller rotating speed is 26 rpm when the ship speed is 5 kts. The ship speed increases to 10 kts when the propeller is rotating at 51 rpm. Detailed information of the DDG 51 ship and P4876 propellers are summarized in Table 1.

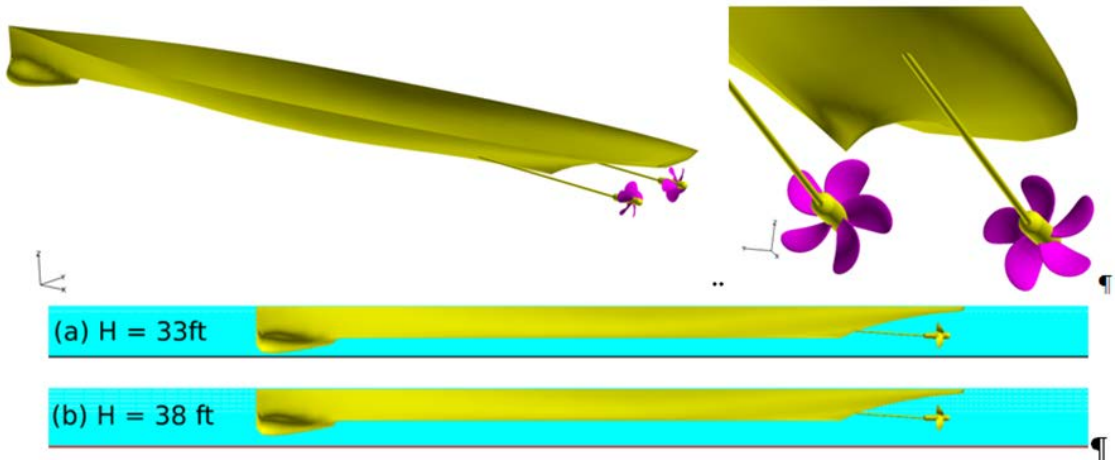

Figure 1. DDG 51 ship and P4876 propeller geometry.

Table 1. Propeller information for DDG 51 ship in FANS simulation.

Case #	1	2	3	4
Ship length L (m)	142.04 (466 ft)	142.04 (466 ft)	142.04 (466 ft)	142.04 (466 ft)
Ship draft (m)	9.4488 (31 ft)	9.4488 (31 ft)	9.4488 (31 ft)	9.4488 (31 ft)
Water depth, H (m)	10.0584 (33 ft)	11.5824 (38 ft)	10.0584 (33 ft)	11.5824 (38 ft)
Underkeel clearance (m)	0.6096 (2 ft)	0.6096 (2 ft)	2.1336 (7 ft)	2.1336 (7 ft)
Propeller diameter, D (m)	5.4864 (18 ft)	5.4864 (18 ft)	5.4864 (18 ft)	5.4864 (18 ft)
Distance between propellers (m)	9.8755 (32.4 ft)	9.8755 (32.4 ft)	9.8755 (32.4 ft)	9.8755 (32.4 ft)
Distance from ship stern to propeller (m)	4.8768 (16 ft)	4.8768 (16 ft)	4.8768 (16 ft)	4.8768 (16 ft)
Propeller depth (depth of the propeller axis)	5.7912 (19 ft)	5.7912 (19 ft)	5.7912 (19 ft)	5.7912 (19 ft)

Table 1. Propeller information for DDG-51 ship in FANS simulation. (Continued)

Case #	1	2	3	4
Distance from center of propeller axis to bottom	4.2672 (14 ft)	4.2672 (14 ft)	5.7912 (19 ft)	5.7912 (19 ft)
Forward Thrust (N)	47314	47314	175307	175307
Ship speed (knots)	5	5	10	10
Propeller rpm, n	26	26	51	51
Propeller advance coefficient	1.082	1.082	1.103	1.103
Characteristic velocity, nD (m/s)	2.3774	2.3774	4.6634	4.6634
Reynolds number based on propeller diameter D	1.115×10^7	1.115×10^7	2.187×10^7	2.187×10^7
Reynolds number based on ship length L	3.262×10^8	3.262×10^8	6.245×10^8	3.262×10^8

2.1 FANS MODEL SIMULATION RESULTS FOR DDG 51 SHIP

Figure 2 shows the computational domain and multi-block overset grids used in this study. The overset grid system consists of 15 computational blocks and 7 phantom grid blocks with 2,369,549 grid points covering half of the solution domain. A near-wall spacing of 5.4864×10^{-6} m was used near the sea bottom to provide accurate resolution of the turbulent boundary layer flow. Since the first grid point is located within the laminar sublayer, it allows us to calculate the shear stresses on the seabed directly without relying on the wall-function approximations.

All calculations were performed for 4,000 time steps (i.e., 100 propeller revolutions) using 12 CPUs on a Linux® cluster. For the 5-kt cases, the ship travels 230.8 s and 594 m. When the ship speed was increased to 10 kts, it took approximately 117.7 secs for the ship to travel 605 m over 100 propeller revolutions. The simulation results clearly indicated that the propeller-induced shear stresses reached a periodic pattern in less than 50 propeller revolutions.

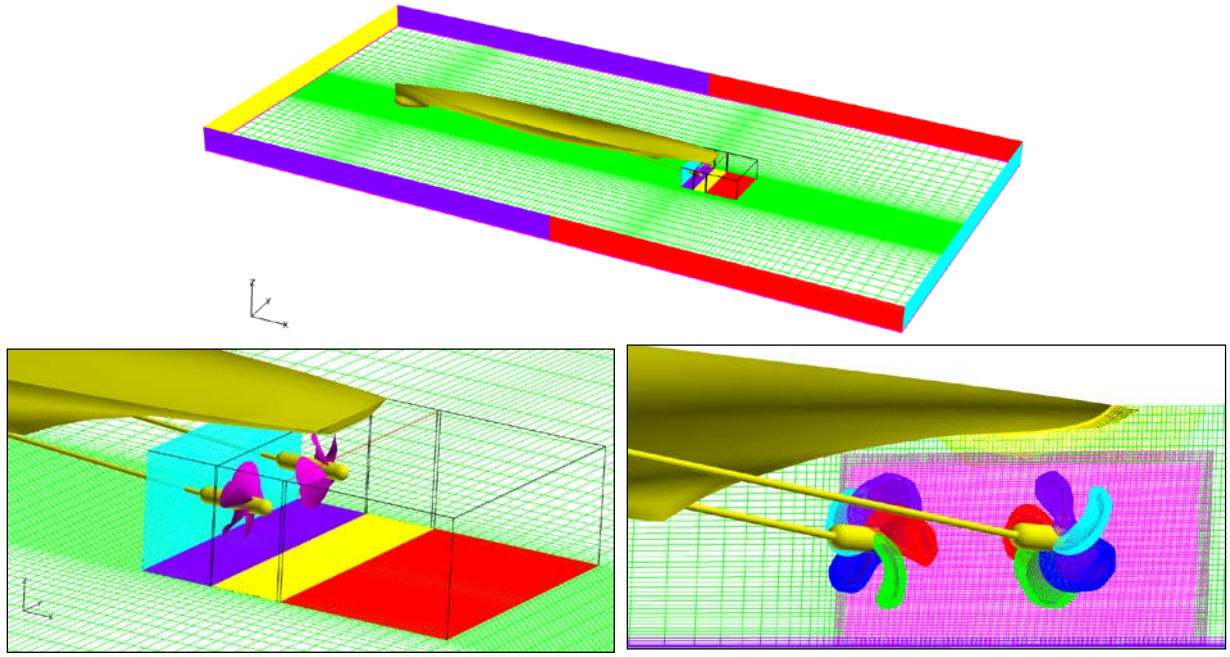

Figure 2. Computational domain and numerical grids.

2.2 DISTURBED VELOCITY PROFILES

Figure 3 shows the predicted velocity contours and velocity vectors adjacent to the sea bottom. For completeness, the velocity vectors at the keel plane is also shown in Figure 4 to provide a more detailed understanding of the three-dimensional flow field induced by the ship motions. For simplicity, the velocities are normalized by a characteristic velocity V_o = nD given in Table 1, where n is the propeller rotating speed (rps) and D is the propeller diameter (m). Note that the ship is traveling in the negative x-direction on an earth-fixed frame. This is equivalent to a positive current in the x-direction on a ship-fixed reference frame. Figures 3 and 4 clearly show that a strong flow acceleration exists beneath the sonar dome when the water is forced to pass through the narrow underkeel clearance below the sonar dome. This acceleration resulted in positive velocities (in the opposite direction of the ship motion) and high shear stresses beneath the sonar dome.

Figures 4(b) and 4(d) show that for the deep water cases with H = 11.5824 m, a significant portion of the flow is pushed underneath the bow due to local flow acceleration around the sonar dome. This produces a large flow recirculation region (in earth-fixed reference frame) at the keel plane, with a fairly weak return flow near the sea bottom.

When the water depth was reduced to H = 10.0584 m, a much larger resistance pushes the flow beneath the sonar dome. Consequently, most of the surrounding water tends to move laterally around the sonar dome and the flow recirculation near the seabed was confined to a fairly small region immediately downstream of the bow, as shown in Figures 4(a) and 4(c). Figures 3(a) and 3(c) clearly show that the ship induced a strong trailing water flow (in the same direction of the ship motion) beneath the ship keel, which extends beyond the propeller plane and well into the far wake. The high velocity (and high shear stress) regions around the bow and mid-ship are induced by the ship hull movement, but not directly related to the propeller wash. Note that the effect of propeller thrust and torque are confined to the ship stern and wake regions.

Figure 5 shows the propeller-induced velocity distribution along the center plane of the propeller axis. The axial velocity contours at five selected cross-sections are also shown in Figure 6 to provide a better understanding of the swirling flow pattern induced by the propeller rotation. The figure shows that the propeller rotation induced strong swirling flow immediately downstream of the propeller. The axial flow induced by the propeller thrust force remains strong for more than 15 propeller diameters behind the ship stern, though we used a rather coarse grid in the far wake. This strong axial flow is expected to carry the suspended sediment for a long distance downstream of the twin-screw propellers.

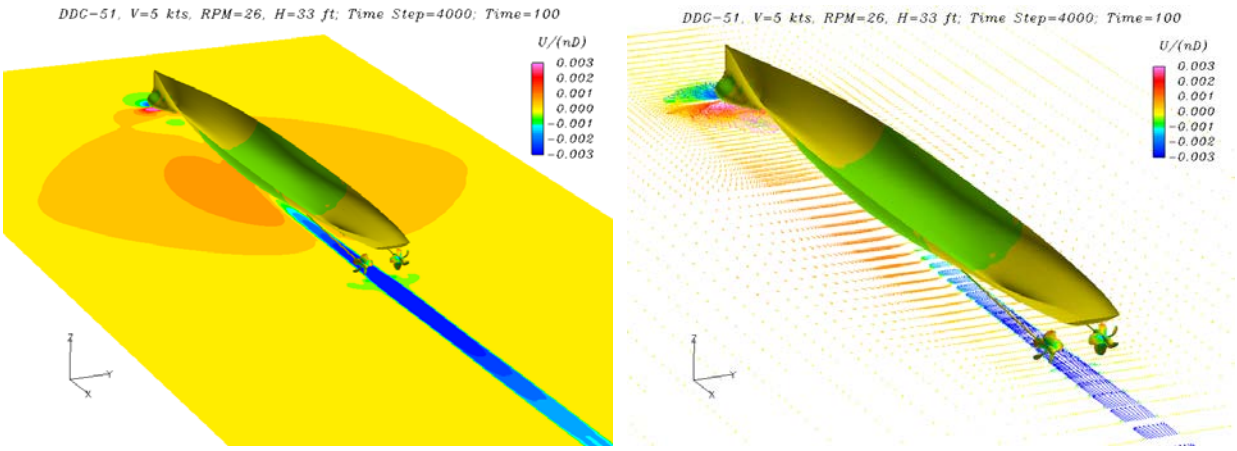

(a) Case 1: V = 5 kts, H = 10.0584 m, ω = 26 rpm.

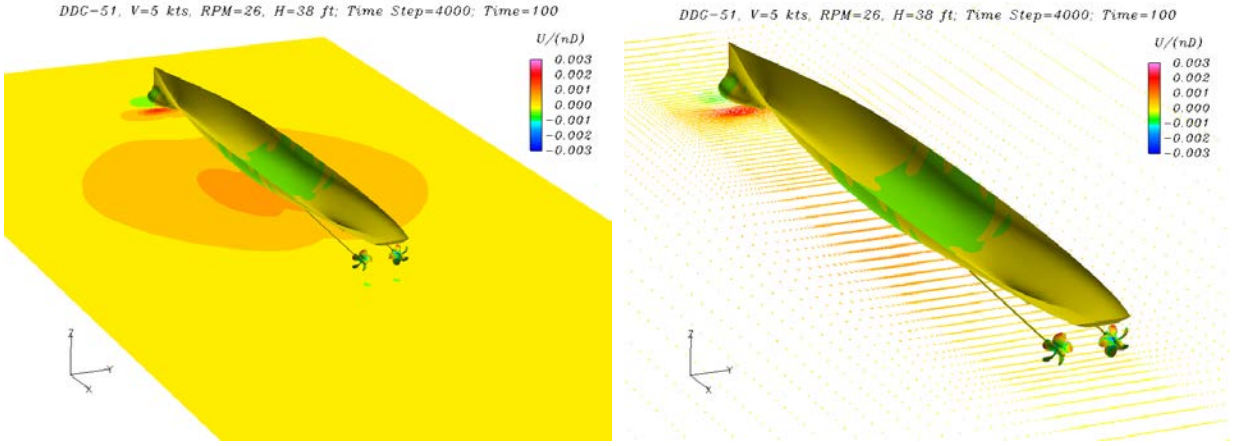

(b) Case 2: V = 5 kts, H = 11.5824 m, ω = 26 rpm.

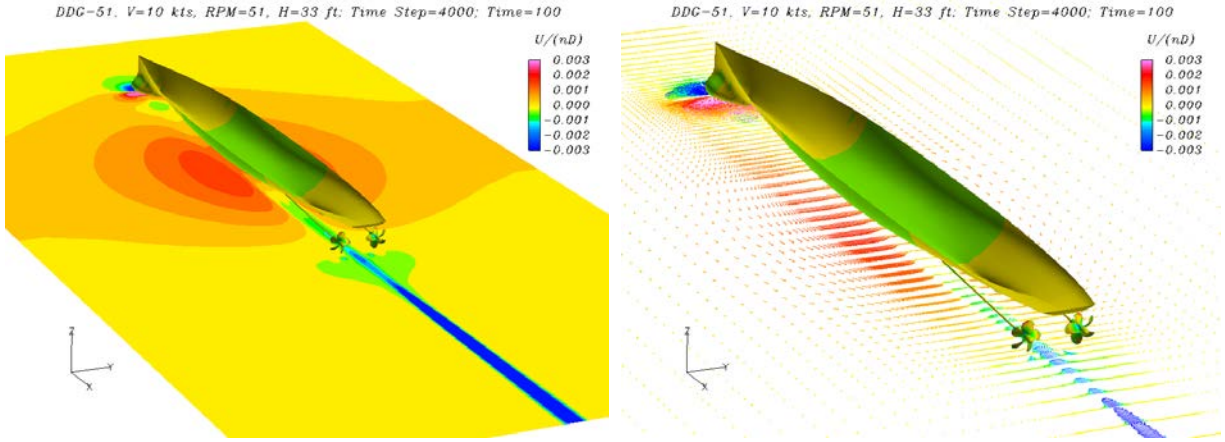

(c) Case 3: V=10 kts, H=10.0584 m, ω = 51 rpm.

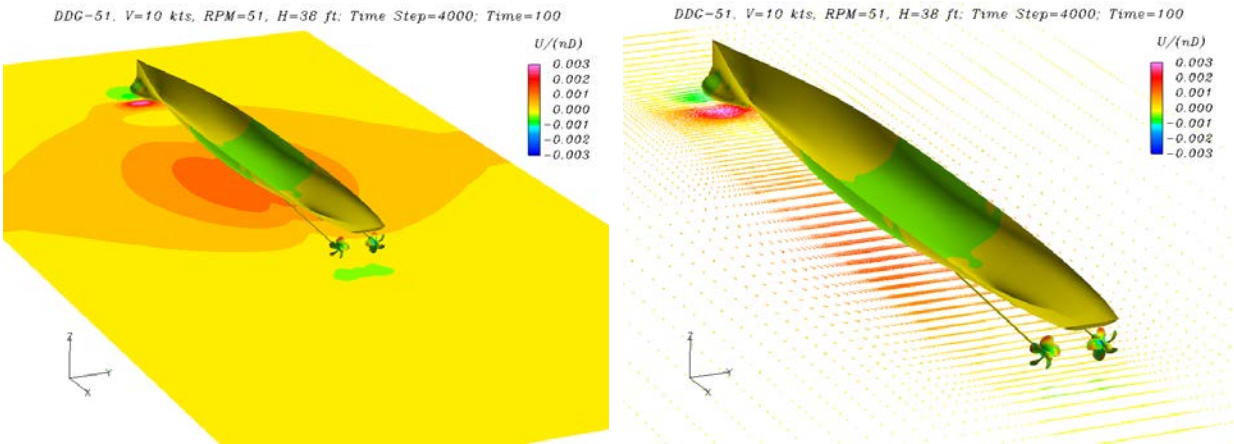

(d) Case 4: V = 10 kts, H = 11.5824 m, ω = 51 rpm.

Figure 3. Longitudinal velocity contours and velocity vectors near seabed.

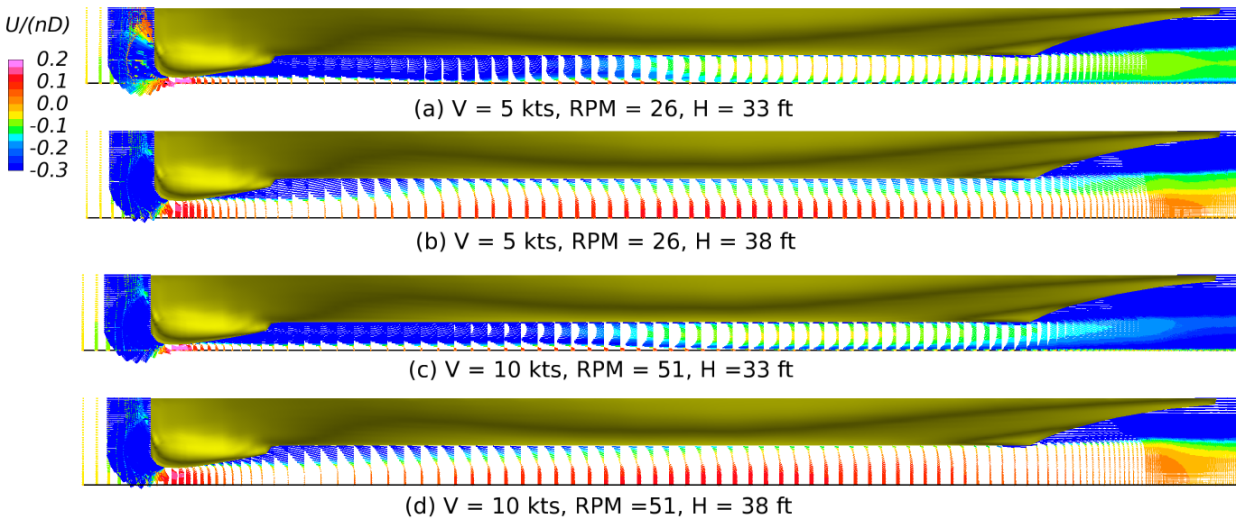

Figure 4. Velocity profiles at the keel plane.

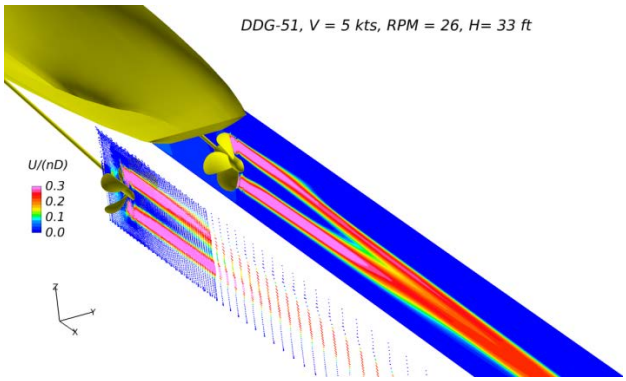

(a) Case 1: V = 5 kts, H = 10.0584 m.

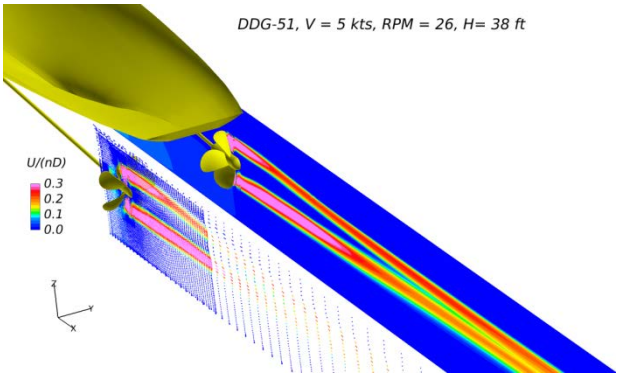

(b) Case 2: V = 5 kts, H = 11.5824 m.

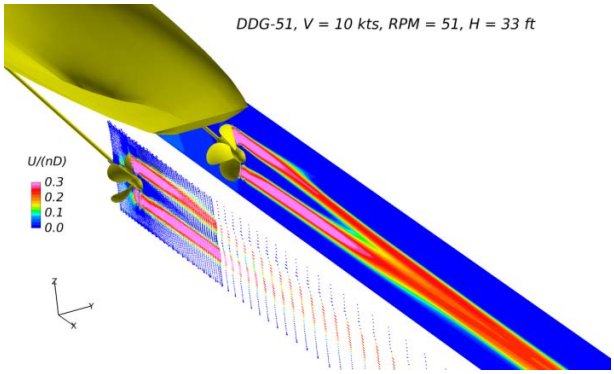

(c) Case 3: V = 10 kts, H = 10.0584 m.

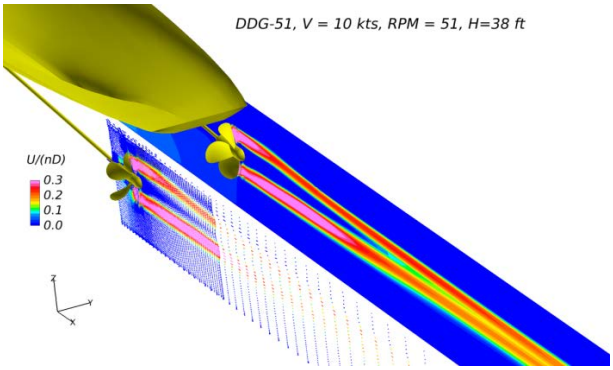

(d) Case 4: V = 10 kts, H = 11.5824 m.

Figure 5. Axial velocity contours and velocity vector plots around the propeller.

In addition to the axial flow profiles in Figures 5 and 6, the swirling flows at selected cross-sections are also shown in Figure 7 to provide a complete description of the three-dimensional flow field induced by the propeller rotation. The figures show that the propeller-induced swirling flow patterns are quite similar immediately downstream of the propeller. However, the propeller swirl is somewhat stronger in the far wake for shallow-water cases with H = 10.0584 m. Note that a second pair of counter-rotating vortices are near the center plane of symmetry. This vortex pair was generated in the narrow gap region around the sonar dome and remains visible in the far wake.

A detailed examination of the velocity profiles near sea bottom (see Figures 3 and 4) indicated that the propeller wash effect is negligible for the deep water cases since the swirling flow decreases quickly in the radial direction away from the propeller tip as shown in Figure 7. The effect of propeller wash grew considerably stronger under shallow-water conditions when the minimum gap below the propeller tip was reduced from 3.048 m (10 ft) to 1.524 m (5 ft).

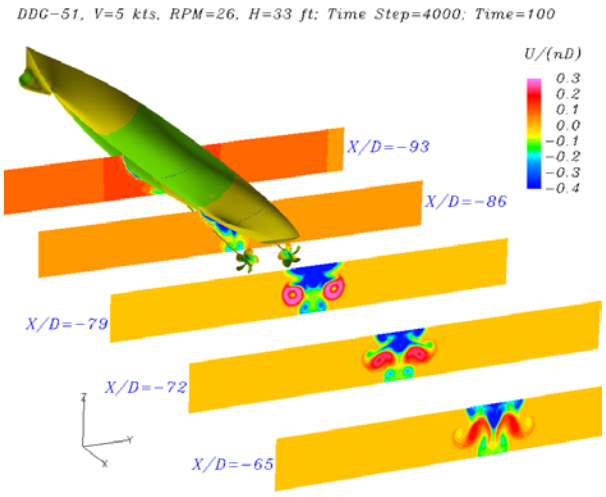

(a) Case 1: V = 5 kts, H = 10.0584 m.

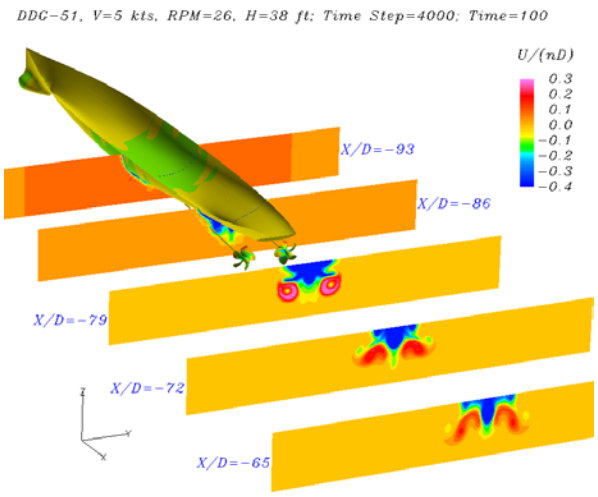

(b) Case 2: V = 5 kts, H = 11.5824 m.

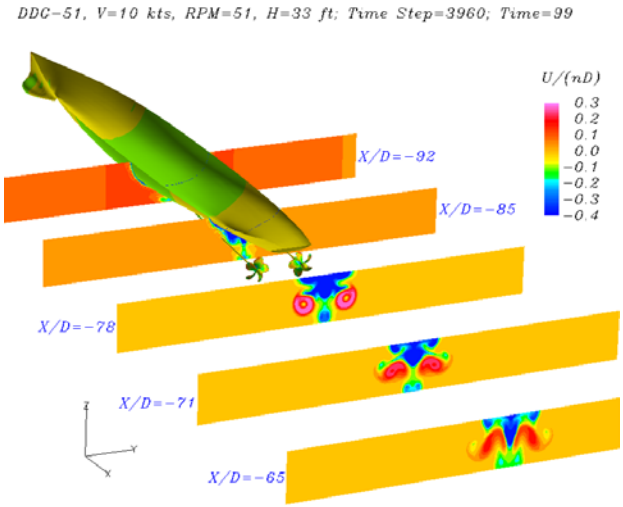

(c) Case 3: V = 10 kts, H = 10.0584 m.

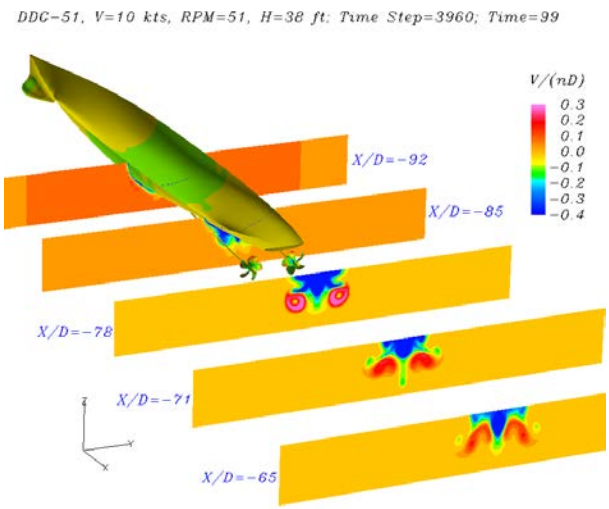

(d) Case 4: V = 10 kts, H =11.5824 m.

Figure 6. Propeller-induced flow field at selected stations.

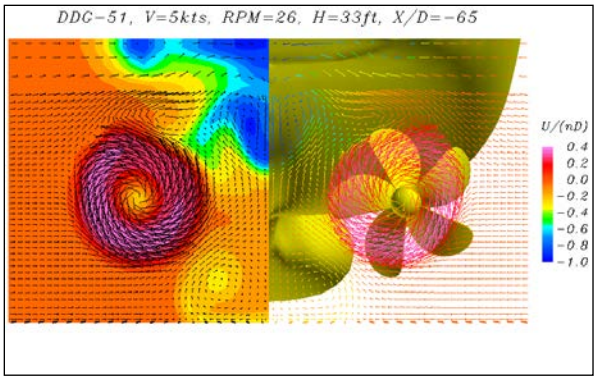

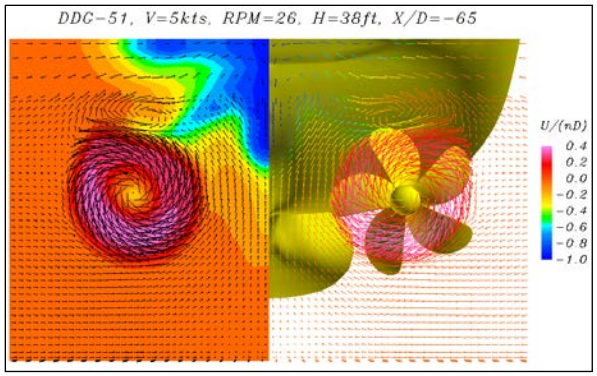

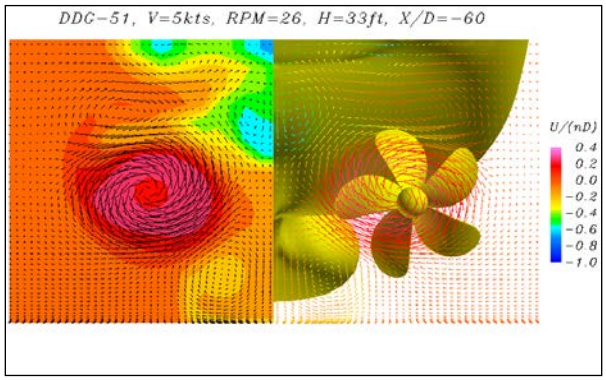

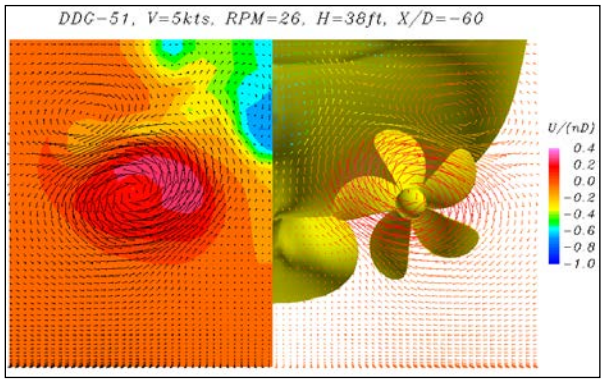

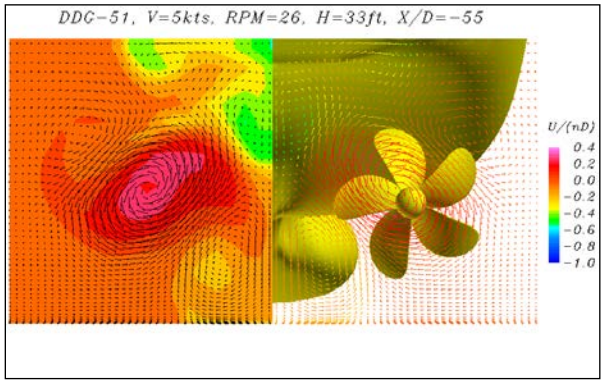

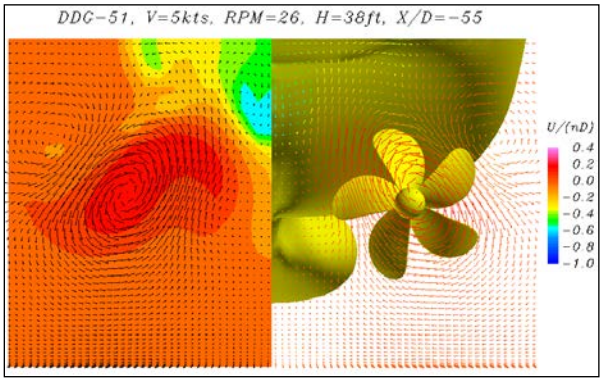

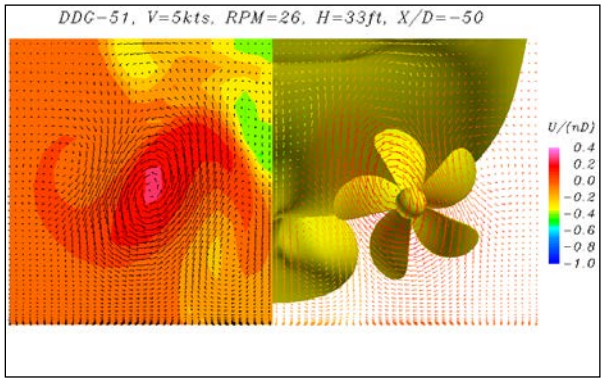

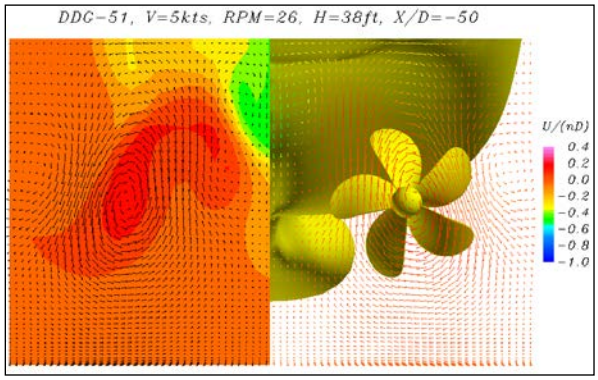

(a) Case 1: V = 5 kts, H = 10.0584 m.

(b) Case 2: V = 5 kts, H =11.5824 m.

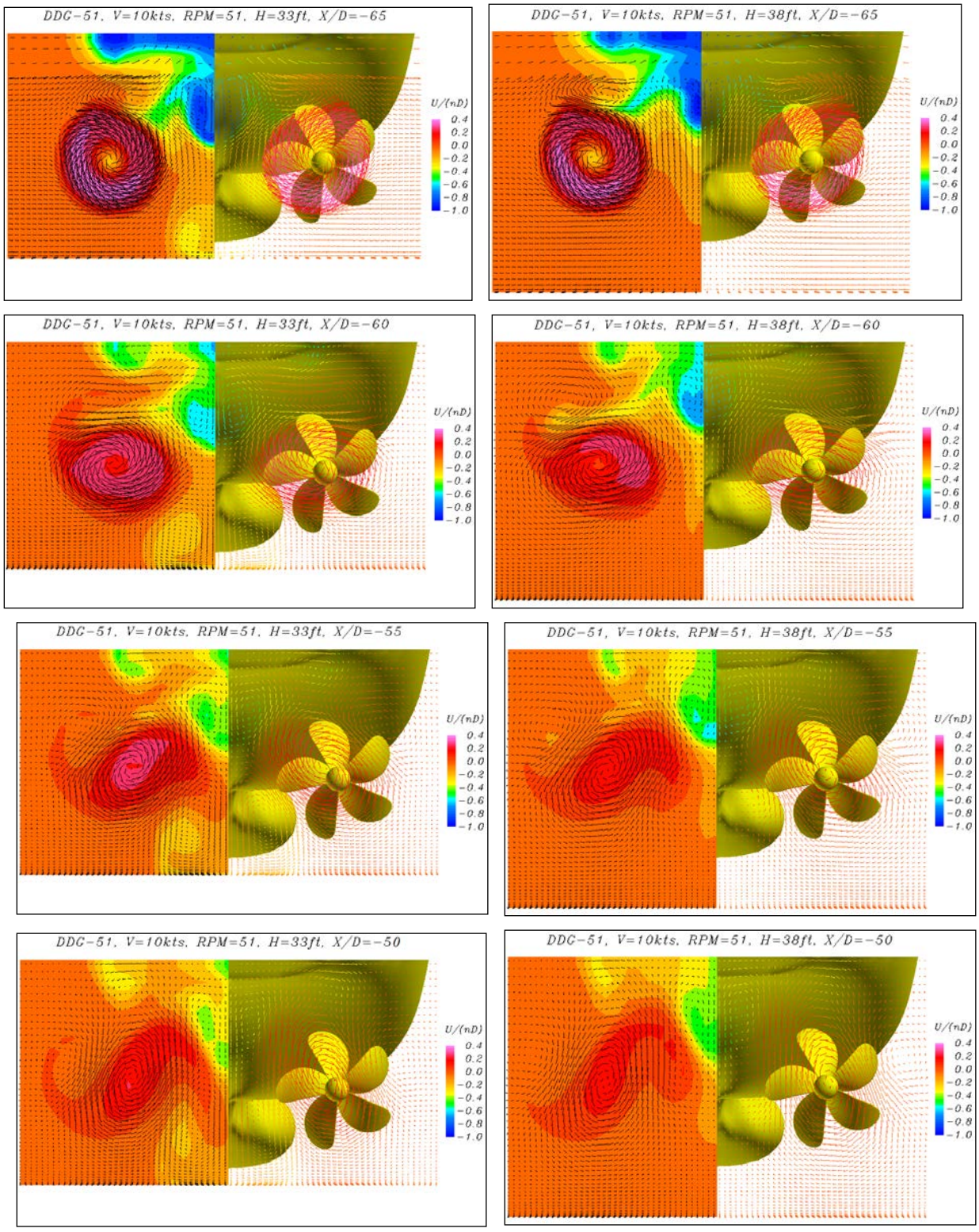

(c) Case 3: V = 10 kts, H =10.0584 m. (d) Case 4: V = 10 kts, H = 11.5824 m.

Figure 7. Propeller-induced swirling flows.

2.3 ESTIMATED BOTTOM SHEAR STRESSES

Figure 8 shows the shear stress distributions on the sea bottom for all four test cases considered in the current study. Note that different color bar scales were used since the bottom shear stresses for Case 2 are considerably smaller than the other three cases. In general, the bottom shear stress increases with the propeller revolutions per minute and ship speed. Under deep-water conditions, the maximum shear stress occurred beneath the sonar dome due to strong flow acceleration through the narrow passage between the sonar dome and sea bottom. High shear stress regions were also observed around the mid-ship due to large block coefficient of the DDG-51 hull cross-section area. The propeller-induced shear stresses are not as high as those induced by the ship motion. Furthermore, the propeller wash effects are confined to a rather small region directly below the twin-screw propellers. For shallow-water cases with H = 10.0584 m, the highest shear stress also occurred underneath the sonar dome. However, the shear stresses in the stern region are also very high due to the presence of strong underkeel current (see Figure 4) induced by the ship motion.

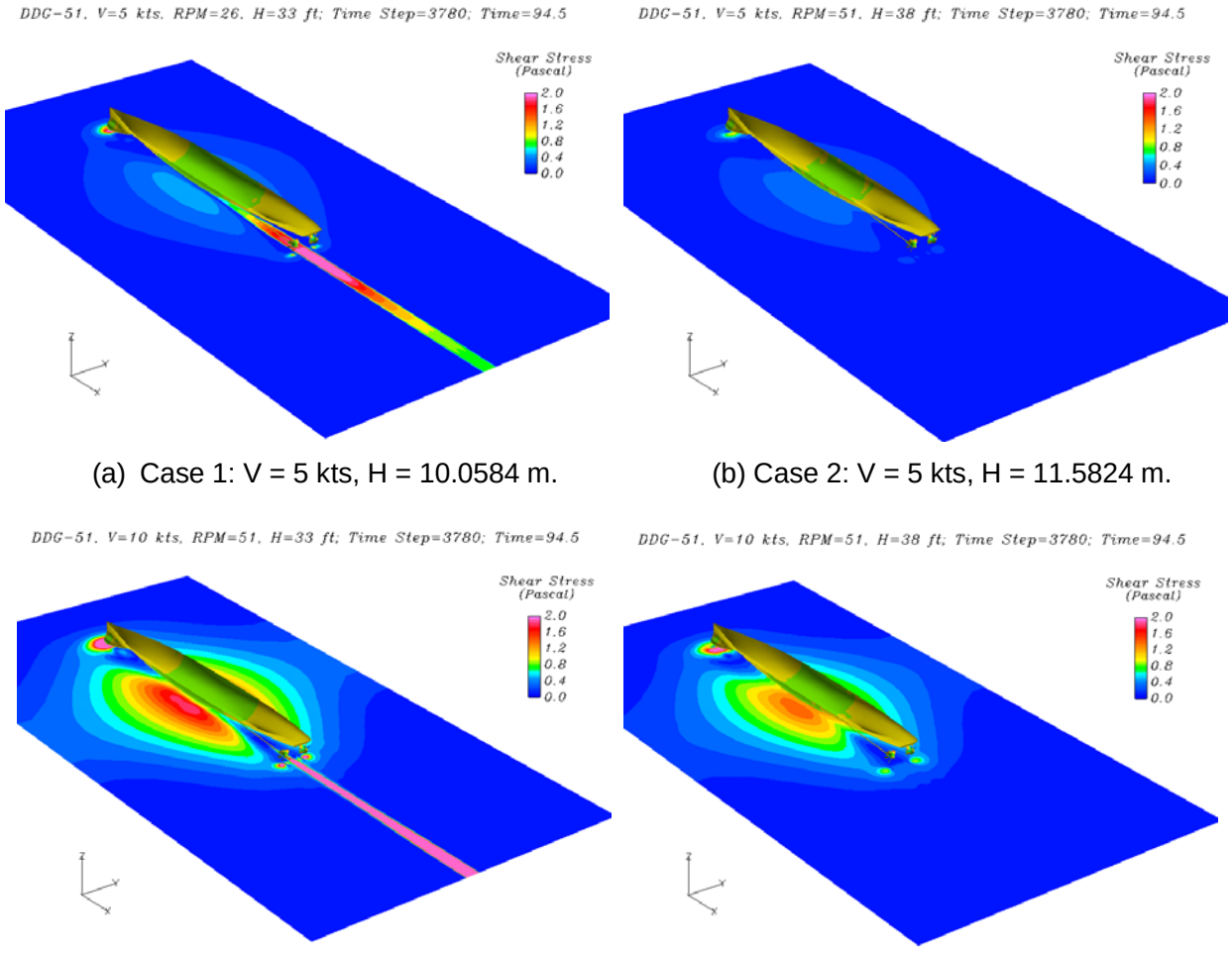

(a) Case 1: V = 5 kts, H = 10.0584 m.

(b) Case 2: V = 5 kts, H = 11.5824 m.

(c) Case 3,:V = 10 kts, H = 10.0584 m.

(d) Case 4: V = 10 kts, H = 11.5824 m.

Figure 8. Shear stress distribution on the seabed.

Figure 9 shows the surface plots of seabed shear stress distributions under different water depths and different ship speeds. For clarity, the shear stress scales were adjusted for each case to provide a detailed comparison of the shear stress patterns in the bow, mid-ship, propeller, and ship stern

regions. As noted earlier, the highest shear stress occurred beneath the sonar dome for all four test cases considered. For deeper water cases, the propeller induced shear stresses are considerably smaller than those induced by the ship hull motion. However, the bottom shear stress distributions changed drastically when the water depth was reduced to H = 10.0584 m with a very small underkeel clearance of 0.6096 m. The high shear stresses in the ship wake regions were induced primarily by the trailing water in the narrow gap between the keel and seabed. The simulation results clearly demonstrated that the blockage effect (i.e., block coefficient) of the ship hull in shallow water is the dominant parameter in determining the sea bottom shear stress distributions.

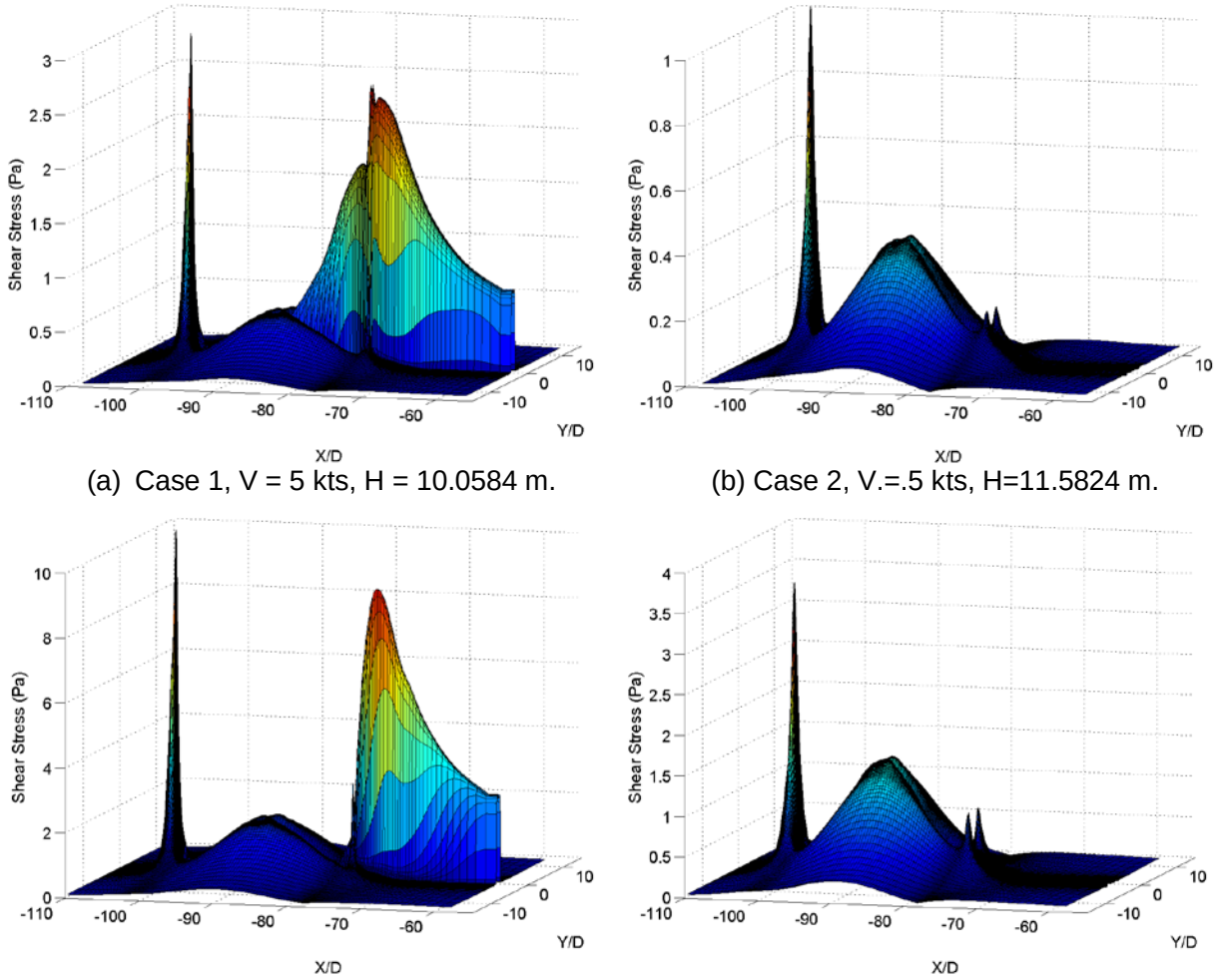

(a) Case 1, V = 5 kts, H = 10.0584 m. (b) Case 2, V.=.5 kts, H=11.5824 m.

(c) Case 3, V = 10 kts, H = 10.0584 m (d) Case 4, V = 10 kts, H = 11.5824 m.

Figure 9. Surface plots of shear stresses on the seabed.

For completeness, enlarged views of the seabed shear stress distributions around the twin-screw propellers and the ship stern regions are also shown in Figure 10 to provide a detailed assessment of the propeller wash effects. In addition, the maximum shear stresses at various locations of the seabed were also summarized in Table 2. The propeller-induced shear stresses are much smaller than the hull-induced shear stresses under shallow-water conditions. The maximum shear stress in the ship wake exceeded 8.9 Pa for Case 3 when the ship speed was 10 kts. Even for the lower speed case with V = 5 kts (Case 1), the bottom shear stress in Case 1 still reached nearly 2.5 Pa in the ship wake. The maximum shear stresses in ship wake region are about 3 times of those induced by the propeller

rotation. It is quite obvious that the large blockage effect of sonar dome under shallow-water condition is the primary cause of the strong trailing water and high shear stresses in the narrow gap between the ship keel and sea bottom. However, the shear stress induced by the ship hull is strongly dependent on the ship size, hull form, and water depth. Therefore, it will be necessary to perform numerical simulations for each individual ship to quantify the water depth effect for different type of ships.

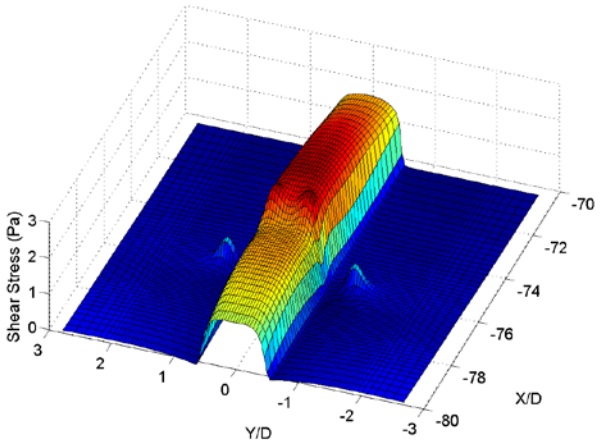

(a) Case 1: V = 5 kts, H = 10.0584 m.

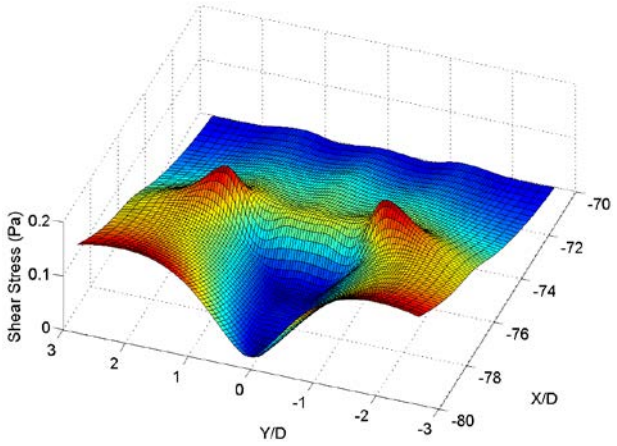

(b) Case 2: V = 5 kts, H = 11.5824 m.

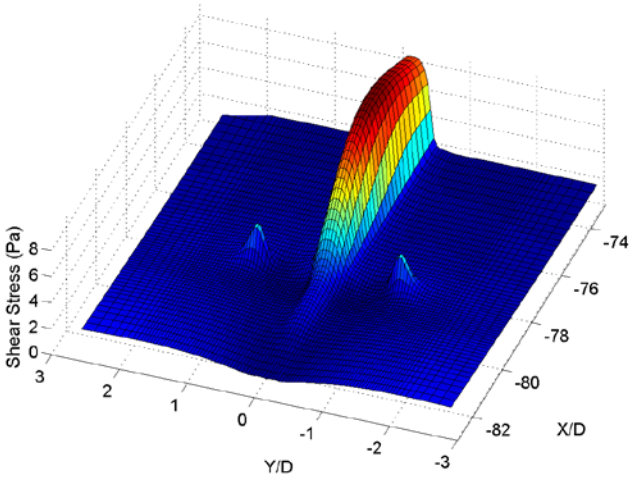

(c) Case 3: V = 10 kts, H = 10.0584 m.

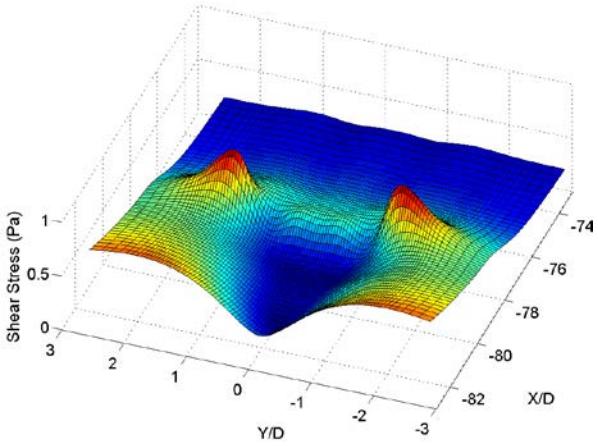

(d) Case 4, V = 10 kts, H = 11.5824 m.

Figure 10. Surface plots of seabed shear stresses around the twin-screw propellers.

Table 2. Maximum shear stresses in different regions of the seabed.

Case #	1 (Pa)	2 (Pa)	3 (Pa)	4 (Pa)
Bow	3.02	1.09	10.53	3.57
Mid-ship	0.51	0.39	1.85	1.46
Propeller	0.85	0.18	3.00	0.85
Ship wake	2.49	0.14	8.94	0.37

3. SIMULATION SCENARIOS FOR TUGBOAT WITH DUCTED PROPELLERS

FANS simulations were also performed for a tugboat with two ducted propellers as shown in Figure 11 at a constant water depth of 9.144 m (30 ft) under three different flow conditions: (1) propeller blowing to open water, (2) propeller blowing toward a pier wall, and (3) propeller blowing parallel to a pier wall. Since the detailed geometries of the tugboat and propellers used in the experiments are not available, it was necessary to use a simple barge-shaped tugboat as shown in Figure 10. The length of the barge is 28.65 m (94 ft), the beam is 10.36 m (34 ft), and the designed draft is 3.35 m (11 ft). Also, the database of a similar ducted propeller was used to represent the actual propellers used in the experiments. The propeller diameter is scaled to 2.286 m (7.5 ft) and the hub diameter is 0.38 m (1.25 ft). The outside shroud diameter is approximately 2.54 m (100 in.). The two ducted propellers are located at a distance of 15.24 m (50 ft) from the tugboat stern, and at a depth of 4.88 m (16 ft) beneath the free surface. The center-to-center spacing between the left and right propellers is 4.88 m (16 ft). The minimum clearance between the shroud and the seabed is approximately 3.00 m (9.83 ft). In all three simulation scenarios, the propellers are operated at 200 rpm under bollard-pull condition with zero forward speed. Detailed information of the barge-shaped tugboat, ducted propellers, and harbor configurations are summarized in Table 3.

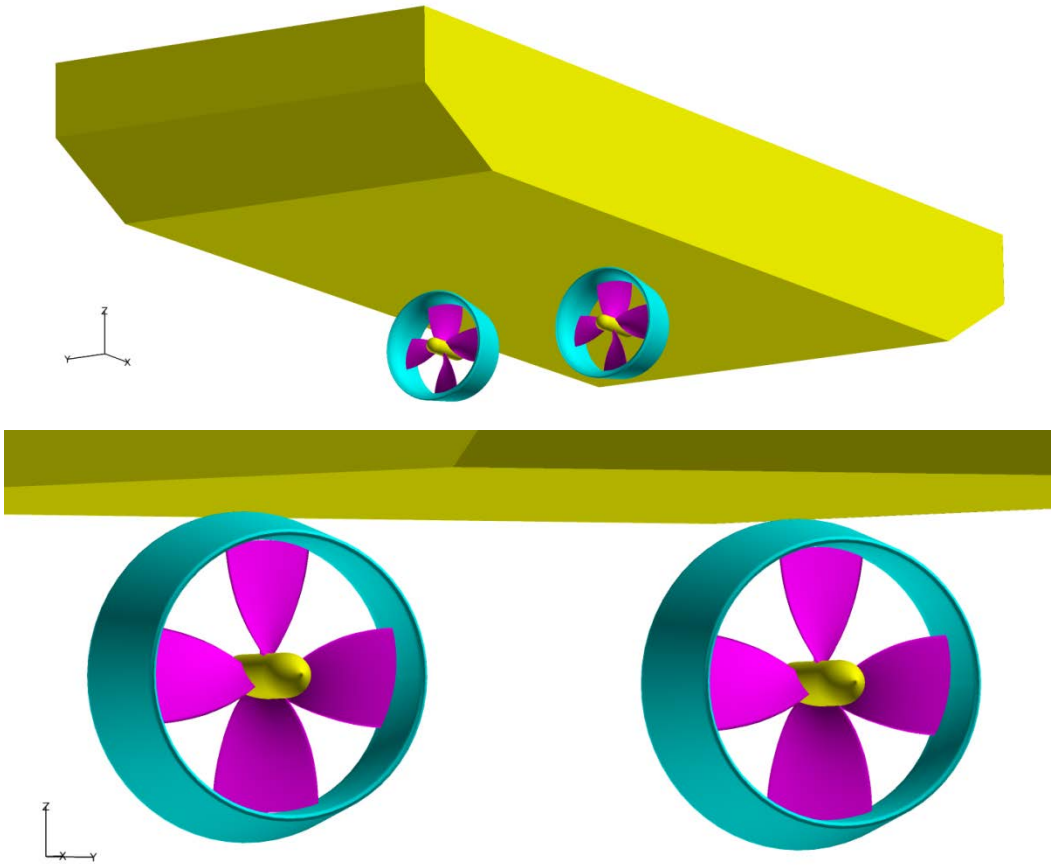

Figure 11. Tugboat and ducted propeller geometry.

Table 3. Propeller information for tugboat in FANS simulation.

Case #	1	2	3
Ship length L (m)	28.65 (94 ft)	28.65 (94 ft)	28.65 (94 ft)
Ship beam B (m)	10.36 (34 ft)	10.36 (34 ft)	10.36 (34 ft)
Ship draft (m)	3.353 (11 ft)	3.353 (11 ft)	3.353 (11 ft)
Water depth, H (m)	9.144 (30 ft)	9.144 (30 ft)	9.144 (30 ft)
Distance from ship bow to pier wall at waterline (m)	1.8288 (6 ft)	Open water	1.8288 (6 ft)
Distance from ship stern to pier wall at waterline (m)	Open water	30.48 m (100 ft)	Open water
Clearance between ship sidewall and pier wall (m)	Open water	Open water	1.524 (5 ft)
Underkeel clearance (m)	2.997 (9.833 ft)	2.997 (9.833 ft)	2.997 (9.833 ft)
Propeller diameter, D (m)	2.286 (7.5 ft)	2.286 (7.5 ft)	2.286 (7.5 ft)
Distance between propellers (m)	4.8768 (16 ft)	4.8768 (16 ft)	4.8768 (16 ft)
Distance from ship stern to propeller (m)	15.24 (50 ft)	15.24 (50 ft)	15.24 (50 ft)
Propeller depth (depth of the propeller axis)	4.8768 (16 ft)	4.8768 (16 ft)	4.8768 (16 ft)
Distance from center of propeller axis to bottom	4.2672 (14 ft)	4.2672 (14 ft)	4.2672 (14 ft)
Ship speed (knots)	0	0	0
Propeller rpm, n	200	200	200
Characteristic time, T_o (s)	0.3	0.3	0.3
Characteristic velocity U_o (m/s)	1.016	1.016	1.106
Reynolds number based on characteristic length L_o (= 1 ft)	2.647×10^5	2.647×10^5	2.647×10^5
Reynolds number based on propeller diameter D	1.488×10^7	1.488×10^7	1.488×10^7

We considered three different harbor configurations in the current tugboat propeller wash study, as shown in Figure 12. In the first test case, the tugboat pushes against a pier wall (with a 1.83-m clearance at the waterline) and the ducted propellers blow to open water. For the second test case, the propeller blows toward a pier wall located at 30.48 m (100 ft) downstream of the ship stern. Note that the distance between the propeller center and the pier wall is 45.72 m (150 ft) since the propeller is located at 15.24 m (50 ft) upstream of the ship stern. The third test case is similar to Case 1, but the tugboat is aligned in parallel to another pier wall, as shown in Figure 12(c). The minimum distance between the tugboat sidewall and the pier wall is 1.52 m (5 ft). As noted earlier, the rotating speed (200 rpm) of the ducted propellers and the water depth (30 ft) remain the same for all three test cases.

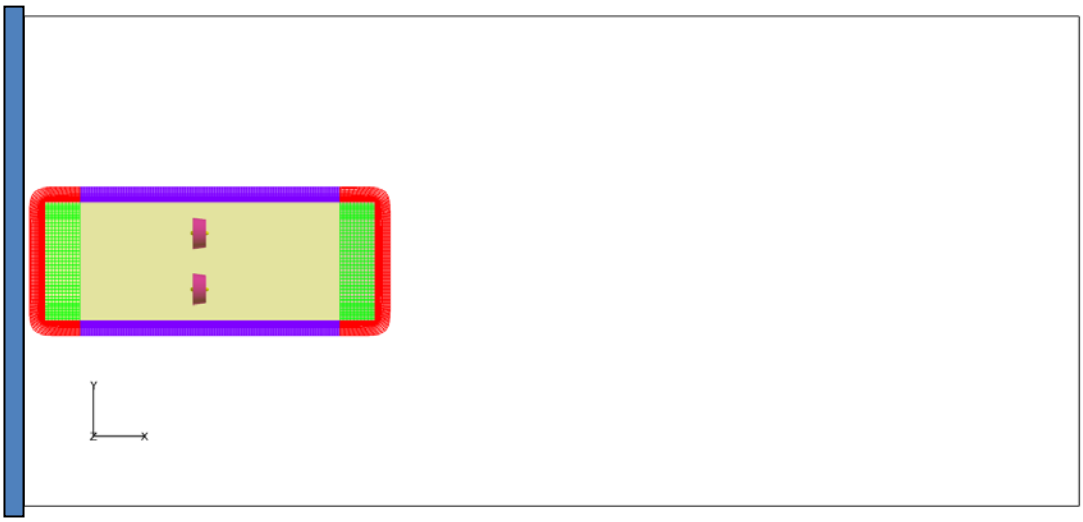

(a) Propeller blowing to open water.

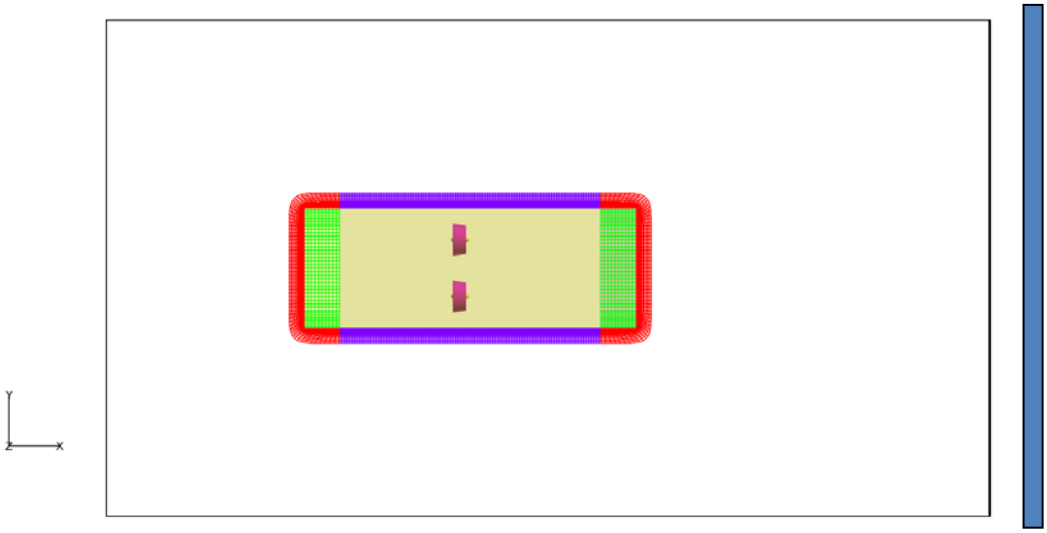

(b) Propeller blowing to pier wall.

(c) Propeller blowing parallel to pier wall.

Figure 12. Harbor configurations for tugboat propeller wash simulations.

3.1 FANS MODEL SIMULATION RESULTS FOR TUGBOAT WITH DUCTED PROPELLERS

Figure 13 shows the computational domain and multi-block overset grids for Case 3 with propeller blowing parallel to the pier wall. The overset grid system consists of 47 computational blocks and nine phantom grid blocks, with 7,070,832 grid points for the entire solution domain. Fourteen grid blocks were used for each ducted propeller to provide detailed resolution of the propeller-induced flow field around the propeller blades, hub, shroud, and near-wake regions. The tugboat is surrounded by a single body-fitted grid block, and the far field is divided into 18 overlapping rectangular grid blocks. The computational load was distributed among 35 CPUs on a Linux® cluster.

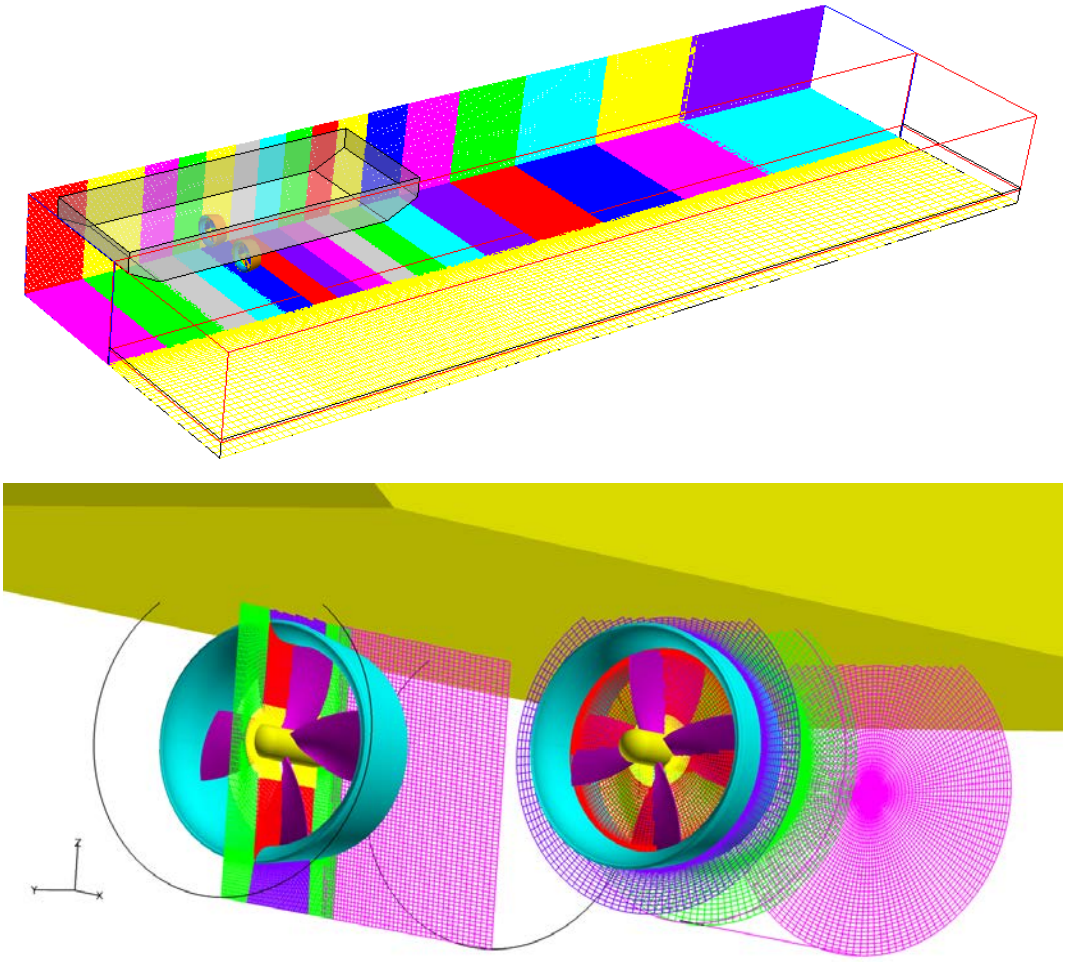

Figure 13. Computational domain and numerical grids.

For simplicity, we performed calculations for Cases 1 and 2 for only one-half the solution domain using Neumann boundary conditions on the plane-of-symmetry (y = 0). The overset grid system for Case 1 consists of 24 computational blocks and 5 phantom grid blocks. The grids around the ducted propeller and the tugboat are identical to those used in Case 3, but only nine computational blocks are needed to cover the far field. There were 3,351,587 grid nodes, and the workload was distributed to 18 CPUs.

The propeller and tugboat grids for Case 2 with propeller blowing toward a pier wall are also identical to those used in Cases 1 and 3. However, we had to refine the far-field grid in front of the

pier wall to provide accurate resolution of the turbulent boundary layer around the pier wall. The overset grid for this case consists of 29 computational blocks and 5 phantom grid blocks, with 14 rectangular grid blocks covering the far field. We used 4,736,735 grid points for one-half of the solution domain, and the workload was distributed among 23 CPUs on a Linux® cluster.

For all three test cases, a near-wall spacing of 3.048×10^{-6} m (10^{-5} ft) was used next to the sea bottom to provide accurate resolution of turbulent boundary layer flow. Since the first grid point is located within the laminar sublayer, it allows us to calculate the shear stresses on the seabed directly without relying on the wall-function approximations. All calculations were performed for 12,500 time steps (i.e., 500 propeller revolutions) with a time increment of 0.012 sec.

3.2 DISTURBED VELOCITY PROFILES

Figures 14 and 15 show the predicted velocity contours on the vertical and horizontal propeller center planes, respectively, for Case 1 with the propeller blowing to open water. For completeness, the velocity contours on the free surface are also shown in Figure 15 to provide a more detailed understanding of the three-dimensional flow field induced by the ducted propellers under a bollard-pull condition. For simplicity, the velocities (U, V, W) are normalized by a characteristic velocity $U_o = nL_o$ given in Table 3, where n is the propeller rotating speed (rps) and the characteristic length L_o is chosen as 0.3048 m (1 ft). Also, the characteristic time is defined as $T_o = L_o/U_o = 1/n$ such that the propeller turns one revolution over one characteristic time. For current simulations with the propellers rotating at 200 rpm, the corresponding characteristic time and velocity scales are $T_o = 0.3$ sec and $U_o = 1.016$ m, respectively.

Figures 14 and 15 clearly show that the propeller wake extends all the way to the downstream edge of the computational domain (about 76 m behind the ducted propellers) in less than 300 propeller revolutions. The propeller wake flow spreads both horizontally and vertically over several propeller diameters. Figure 14 shows that the propeller-induced velocities are considerably stronger near the free surface due to local flow acceleration in the narrow clearance between the propeller blades and the tugboat bottom surface. Note that the tugboat blockage effect is strongly affected by its stern shape and cross-sectional geometry in the propeller wake regions. The blockage effect of the present barge-shaped tugboat tends to be higher than the other ship-shaped tugboats since the block coefficient of a rectangular flat-bottom barge is considerably larger than other tugboat cross-sectional geometries.

As shown in Table 3, the minimum distance between the propeller shroud and the sea bottom is 3.0 m, which is only about 1.3 times of the propeller diameter. Due to the relatively small underkeel clearance, strong propeller-induced current were observed near the sea bottom at approximately 6 to 10 propeller diameters downstream of the propellers during the initial stage of the propeller wash simulation. The high shear stress region extends to more than 20 propeller diameters downstream at a later stage as the propeller wake grows considerably longer and wider after t/To = 400. Note that the propeller-induced flow is highly three-dimensional and strongly affected by the tugboat and sea bottom in confined harbor with shallow water depth.

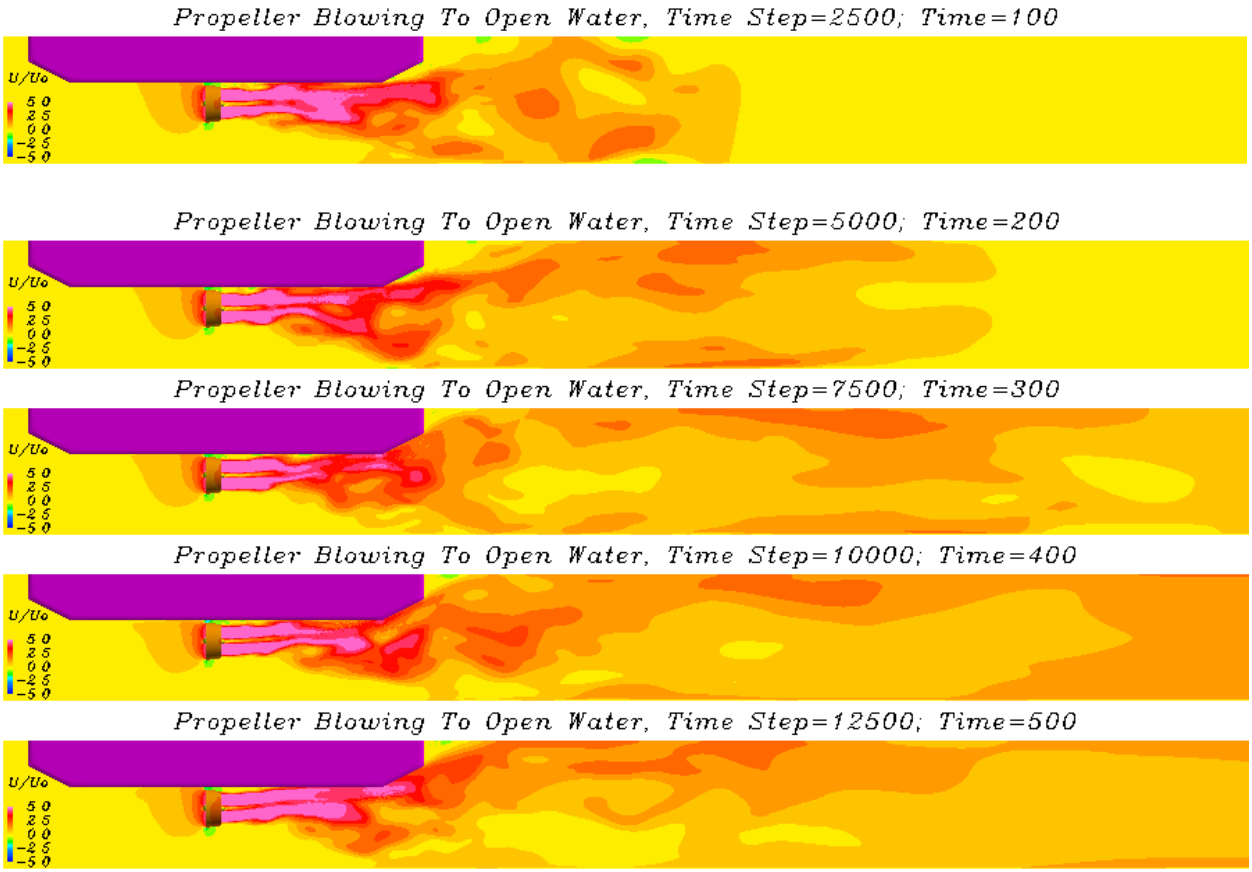

Figure 14. Axial velocity contours on the vertical propeller center plane at t/T_o = 100, 200, 300, 400, and 500 (T_o = 0.3 secs); Case 1 with propeller blowing to open water.

In the second test case, FANS simulation was performed for the same tugboat and ducted propellers in Case 1 but the propellers were blowing to a pier wall located at 30.48 m (100 ft) downstream of the tugboat stern. Figures 16 shows the velocity contours on the vertical propeller center plane, while the velocity contours on the horizontal propeller plane and the free surface are shown in Figure 17. Figure 16 shows that the propeller-induced flow reached the pier wall at about t/To = 132, and was deflected by the pier wall and spread both horizontally and vertically along the pier wall. This produced a stagnation flow region with high impact pressure on the pier wall, as shown in Figure 18.

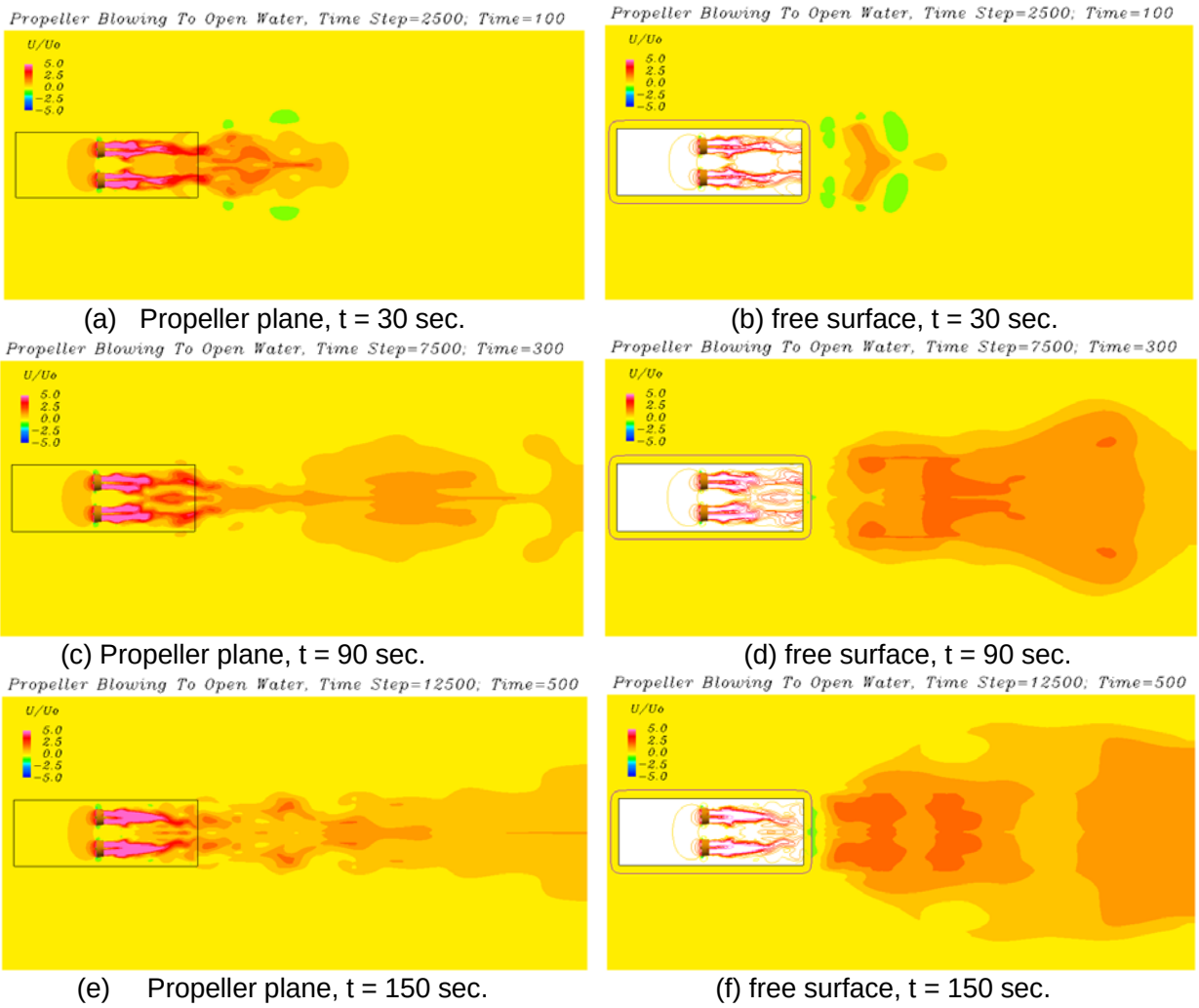

(a) Propeller plane, t = 30 sec. (b) free surface, t = 30 sec.

(c) Propeller plane, t = 90 sec. (d) free surface, t = 90 sec.

(e) Propeller plane, t = 150 sec. (f) free surface, t = 150 sec.

Figure 15. Axial velocity contours on the horizontal propeller center plane (left) and free surface (right) at t/T_o = 100, 300, and 500 (T_o = 0.3 sec); Case 1 with propeller blowing to open water.

In the second test case, FANS simulation was performed for the same tugboat and ducted propellers in Case 1 but the propellers were blowing to a pier wall located at 30.48 m (100 ft) downstream of the tugboat stern. Figures 16 shows the velocity contours on the vertical propeller center plane, while the velocity contours on the horizontal propeller plane and the free surface are shown in Figure 17. Figure 16 shows that the propeller-induced flow reached the pier wall at about t/T_o = 132, and was deflected by the pier wall and spread both horizontally and vertically along the pier wall. This produced a stagnation flow region with high impact pressure on the pier wall, as shown in Figure 18.

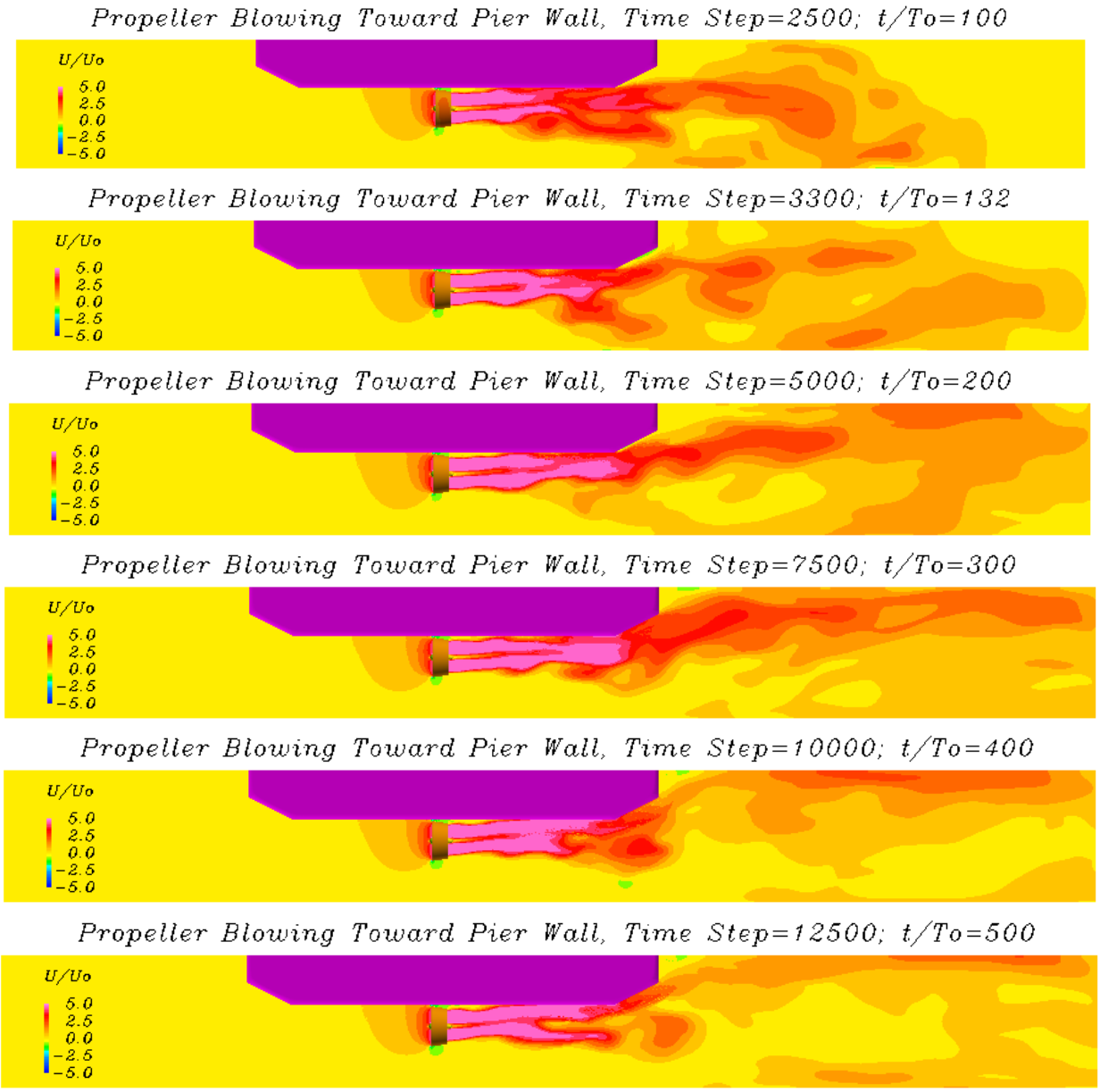

Figure 16. Axial velocity contours on the vertical propeller center plane at t/T_o = 100, 132, 200, 300, 400, and 500 (T_o = 0.3 sec); Case 2 with propeller blowing toward pier wall

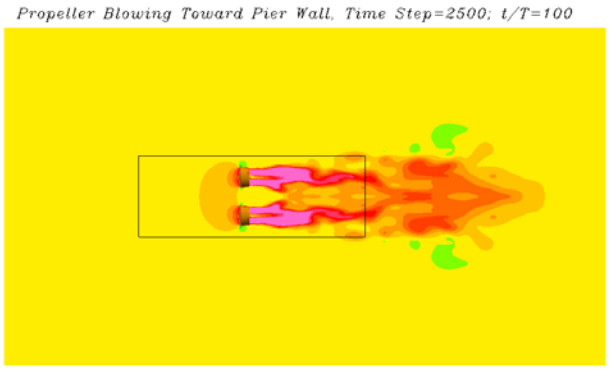

(a) Propeller plane, t = 30 sec.

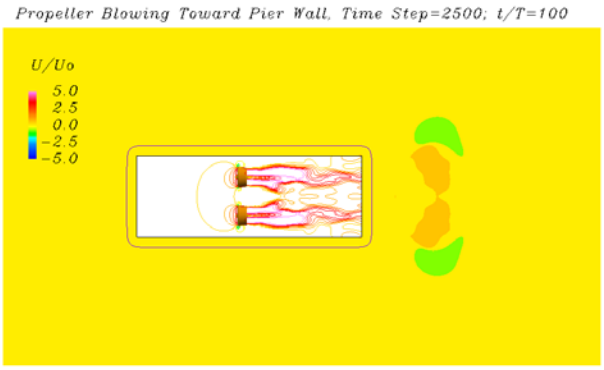

(b) free surface, t = 30 sec.

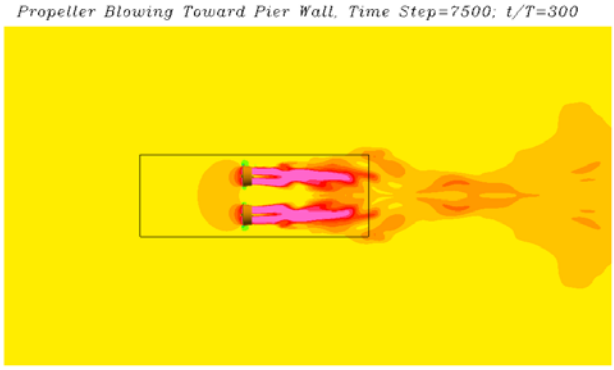

(c) Propeller plane, t = 90 sec.

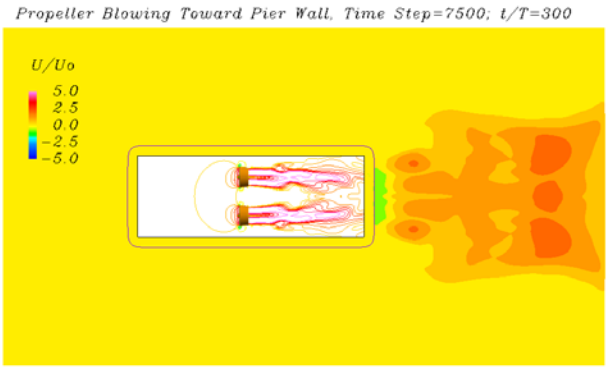

(d) free surface, t = 90 sec.

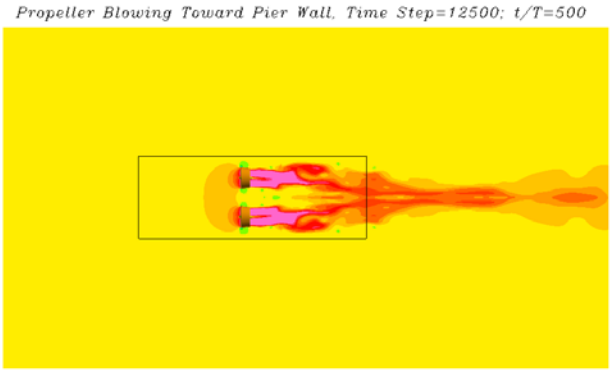

(e) Propeller plane, t = 150 sec.

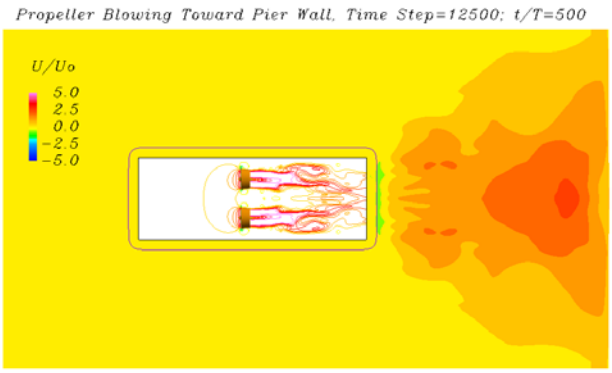

(f) free surface, t = 150 sec.

Figure 17. Axial velocity contours on the horizontal propeller center plane (left) and free surface (right) at t/T_o = 100, 300, and 500 (T_o = 0.3 sec); Case 2 with propeller blowing toward pier wall.

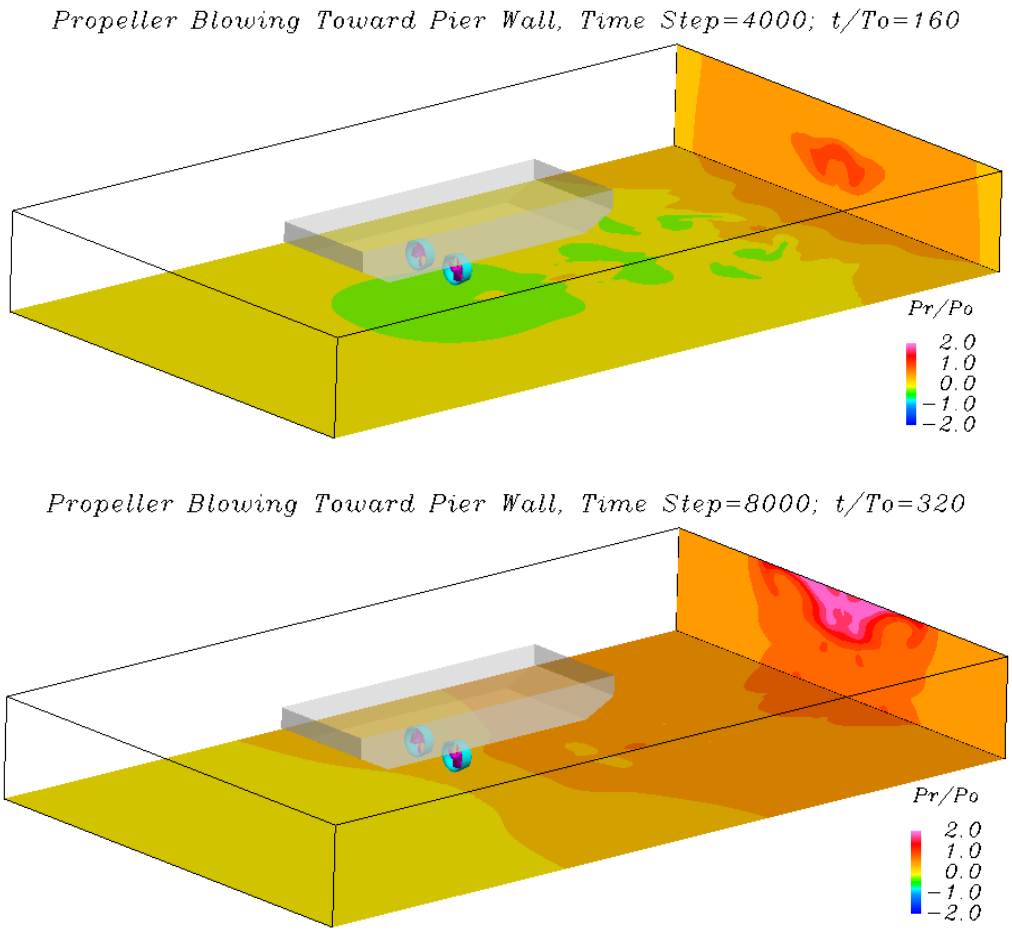

Figure 18. Pressure contours on pier wall and sea bottom, t/T_o = 160 and 320; Case 2 with propeller blowing toward a pier wall.

FANS simulations were also performed for the third test case with the ducted propellers blowing parallel to a pier wall. Due to the asymmetric harbor configuration, it was necessary to calculate the flow over the entire solution domain. Furthermore, unlike the counter-rotating propellers in Cases 1 and 2, we consider two identical right-handed propellers here with both propellers rotating in the same direction. Figures 19 and 20 show the velocity contours on the vertical propeller planes for the right (near pier wall) and left (away from pier wall) propellers, respectively. Furthermore, the velocity contours at horizontal propeller center plane and free surface are also shown in Figure 21 to provide a more detailed description of the complex three-dimensional flow induced by the twin propellers. It is clearly seen that the propeller wake flow is strongly affected by the presence of the parallel pier wall. In general, the velocity induced by the right propeller is much stronger because the propeller-induced radial flow momentum is deflected by the pier wall and redirected toward the axial direction along the pier wall. On the other hand, the wake flow induced by the left propeller is somewhat weaker than those observed in Cases 1 and 2.

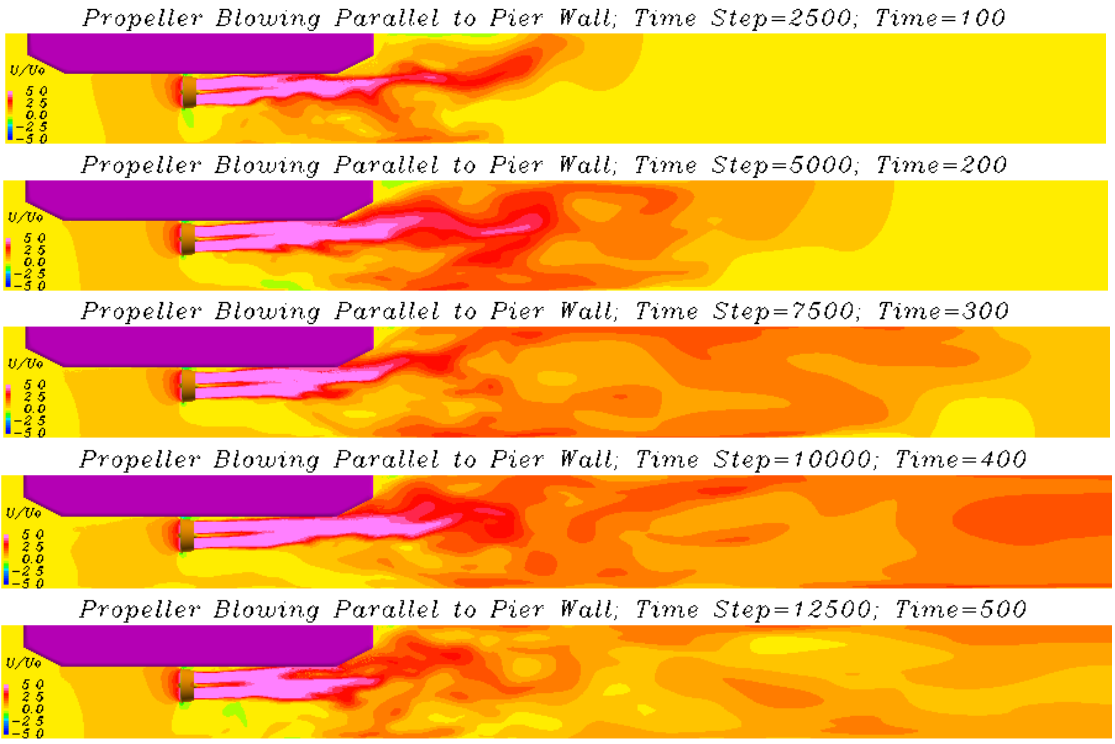

Figure 19. Axial velocity contours behind the right propeller (near pier wall); Case 3 with propeller blowing parallel to pier wall.

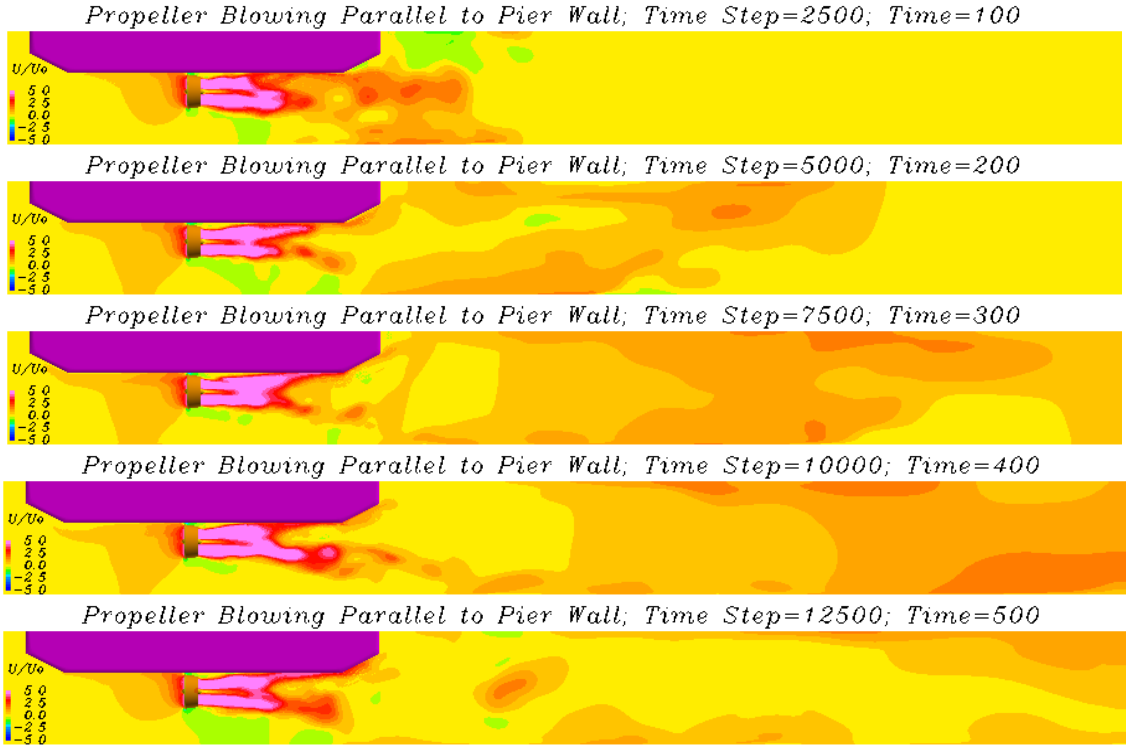

Figure 20. Axial velocity contours behind the left propeller (away from pier wall); Case 3 with propeller blowing parallel to pier wall.

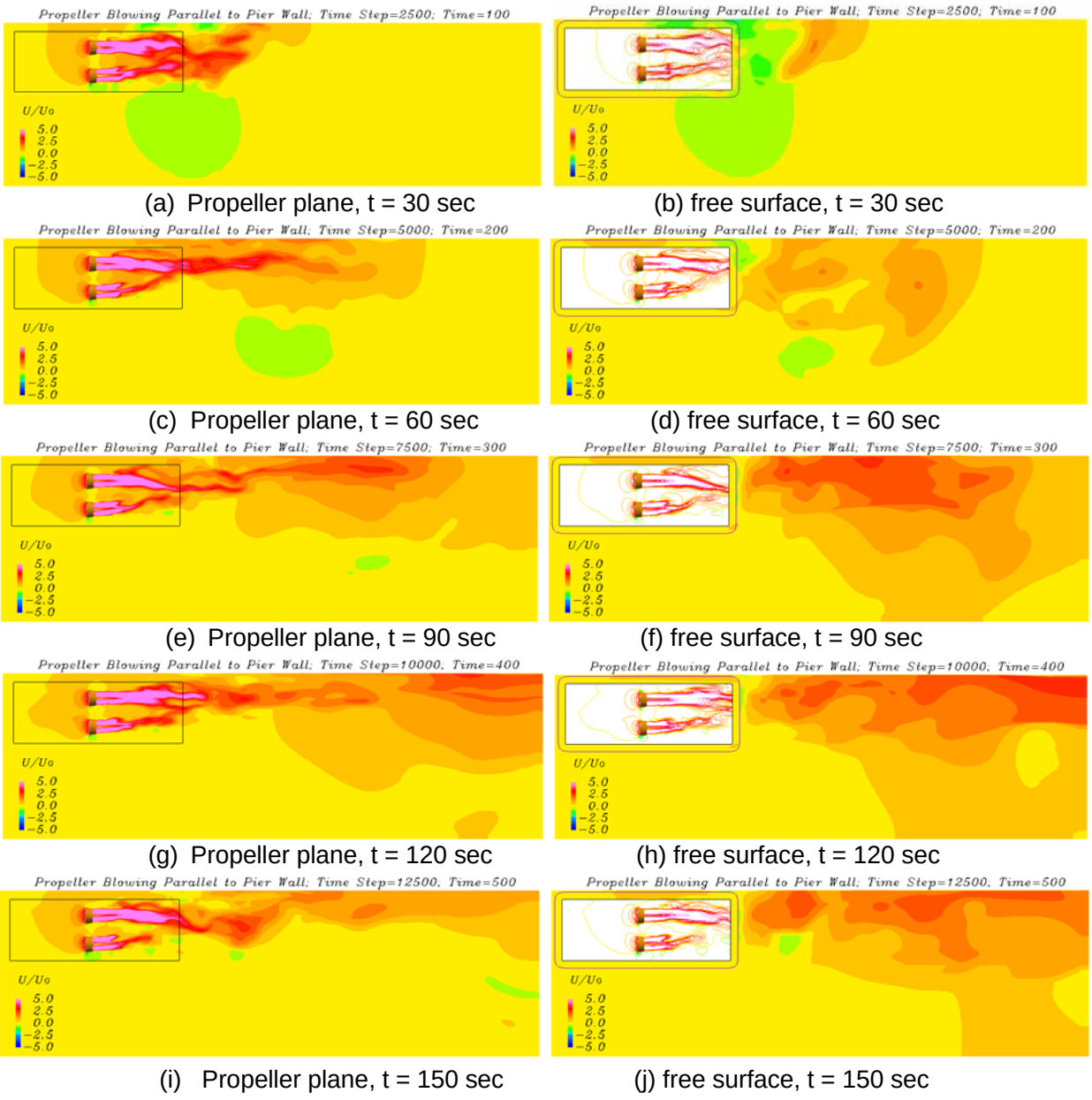

Figure 21. Axial velocity contours on the horizontal propeller center plane (left) and free surface (right) at t/T_o = 100, 200, 300, 400, and 500; Case 3 with propeller blowing parallel to pier wall.

For completeness, three-dimensional views of the propeller-induced flow at the horizontal propeller center plane and four selected axial stations are also shown in Figure 22 to provide a complete description of the propeller wake evolution. The figure clearly shows that the swirling flow behind the right propeller is strongly affected by the pier wall as well as the left propeller. In addition to the deflection of swirling flow momentum by the pier wall, a very strong interaction also exists between the left and right propellers, as shown in Figure 23. For Cases 1 and 2, the propeller-induced swirling flows are affected primarily by the flat bottom surface of the tugboat. For the co-rotating propellers considered in Case 3, however, the swirling flow momentums in the overlap region between two propeller wakes is partially suppressed. This resulted in a deflection of the weaker left propeller wake (away from the pier wall) toward the sea bottom, as shown in Figure 22.

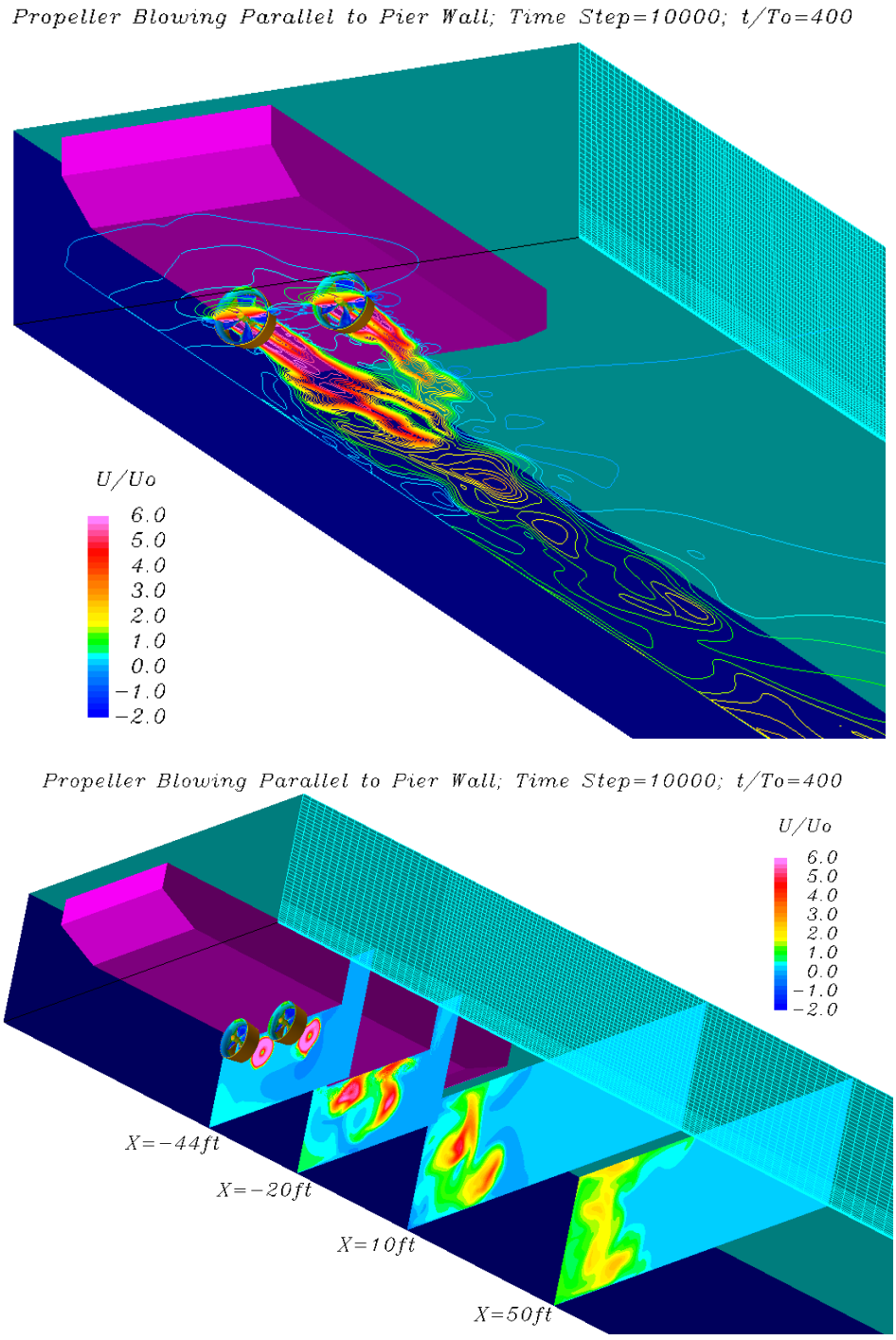

Figure 22. Axial velocity contours at horizontal propeller center plane (top) and selected cross-sections (bottom); Case 3 with propeller blowing parallel to pier wall.

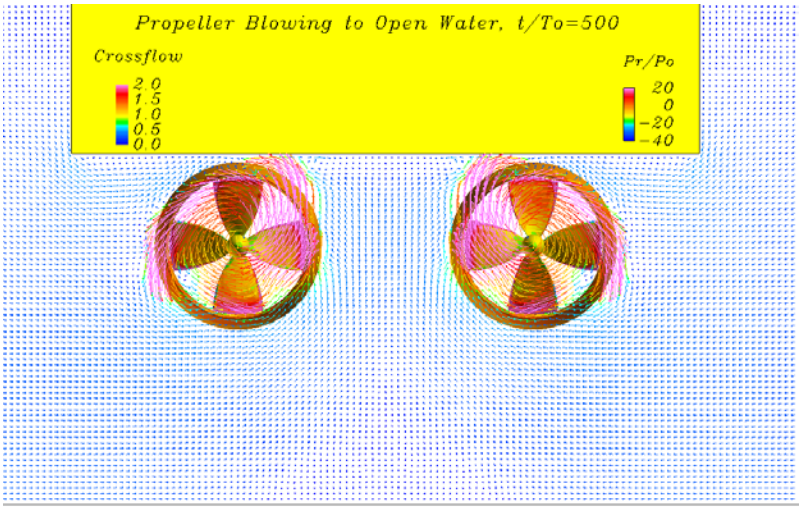

(a) Case 1: X = -12.19 m, t = 150 sec.

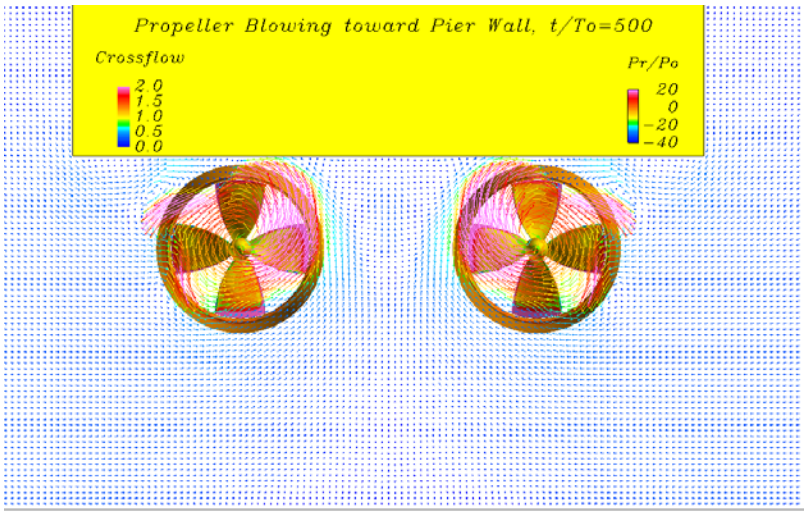

(b) Case 2: X = -12.19 m, t = 150 sec.

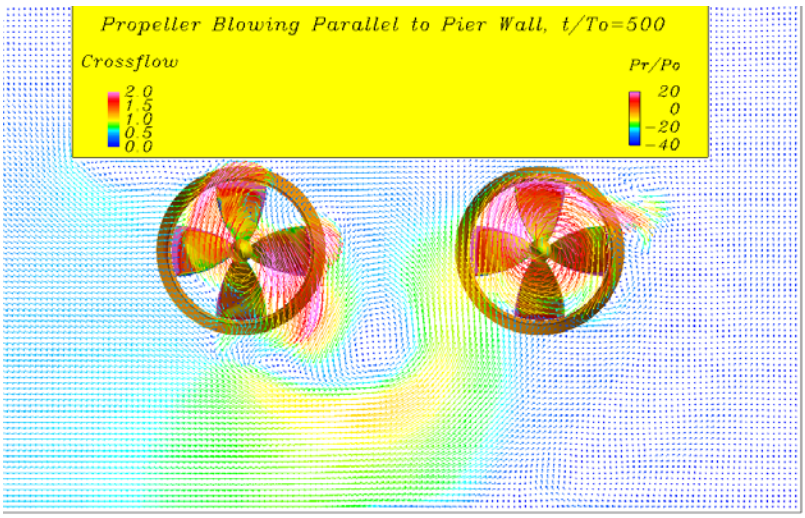

(c) Case 3: X = -12.19 m, t = 150 sec.

Figure 23. Propeller-induced swirling flows (normalized by U_o) at t/T_o = 500.

3.3 ESTIMATED BOTTOM SHEAR STRESSES

Figure 24 shows the shear stress distributions on the sea bottom for Case 1 with propeller blowing to open water. In general, the shear stresses are high during the initial transient period (less than 100 propeller revolutions) after impulsive start of the propeller rotation. As the propeller wakes grow longer and wider, the high shear stress region is pushed downstream and eventually reaches a nearly periodic pattern after 400 to 450 propeller revolutions. At t/T_o = 500, the high shear stress region is observed between 5 to 10 propeller diameters downstream of the propeller and the maximum shear stress is about 4.0 Pa at X/D = 8.9. Note that several high-pressure regions exist because the propeller wake flow is highly unsteady in confined water depth under bollard-pull condition.

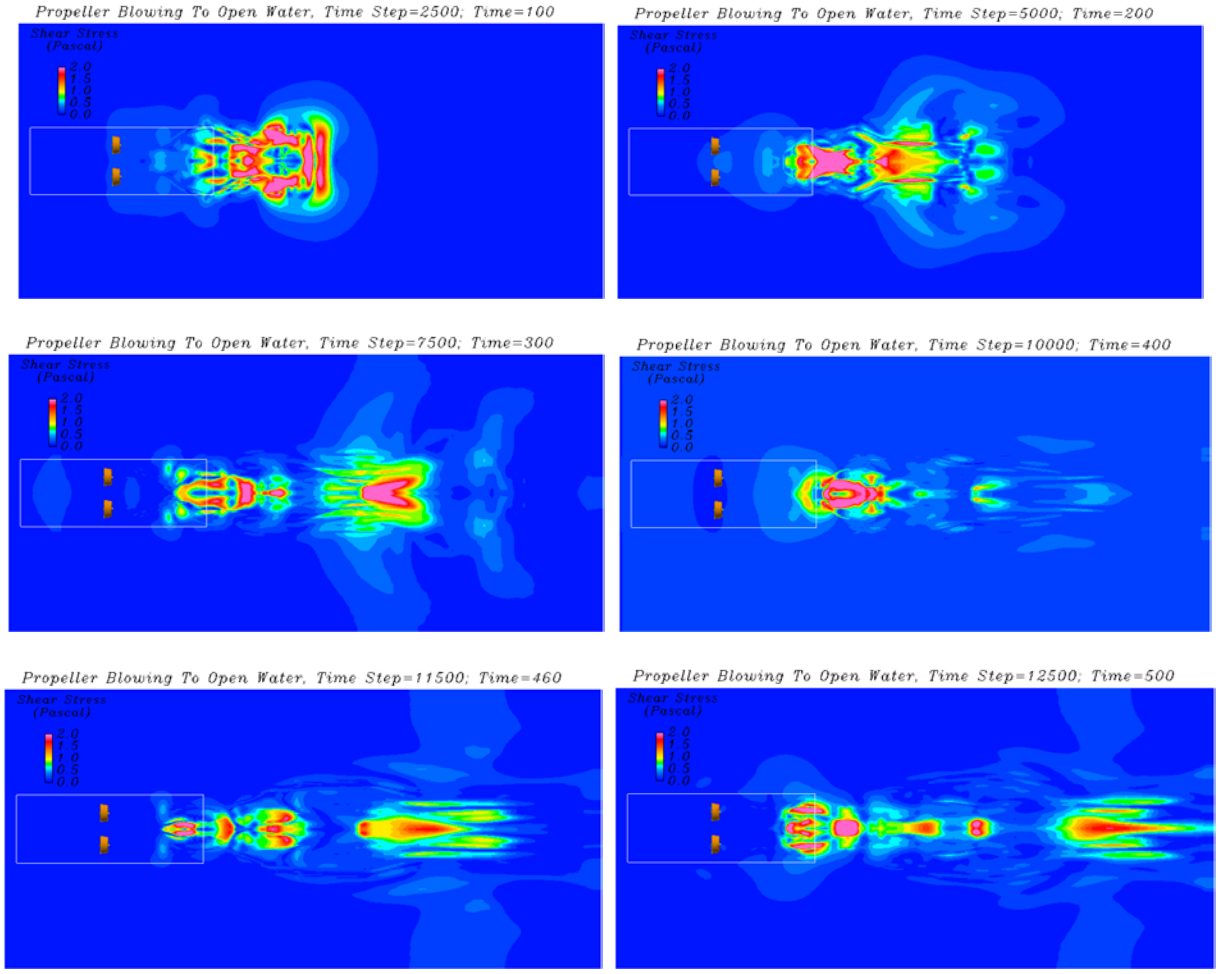

Figure 24. Shear stress distribution on the seabed at t/T_o = 100, 200, 300, 400, 460, and 500; Case 1 with propeller blowing to open water.

Figure 25 shows the shear stress distributions on the sea bottom for Case 2 with propeller blowing to a pier wall. Before the propeller wake reaches the pier wall, the shear stress pattern for Case 2 is similar to that observed in Case 1 with propeller blowing to open water. After the propeller wake impinges on the pier wall at about $t/T_o = 130$, another high shear stress region was developed in front of the pier wall, as seen in Figure 25(c)–(f). As noted earlier, the pier wall forced the propeller wake to spread in both the horizontal and vertical directions. Due to the propeller wake impingement and lateral spread, the high shear stress region gradually shifted downstream. At $t/T_o = 500$, the high shear stress region is observed near the pier wall with a maximum shear stress of about 4.2 Pa at X/D = 15.3 behind the duct propellers. Note that the pier wall drastically altered the shear stress pattern though the maximum shear stress is only slightly higher than that observed earlier in Case 1 with the propellers blowing to open water.

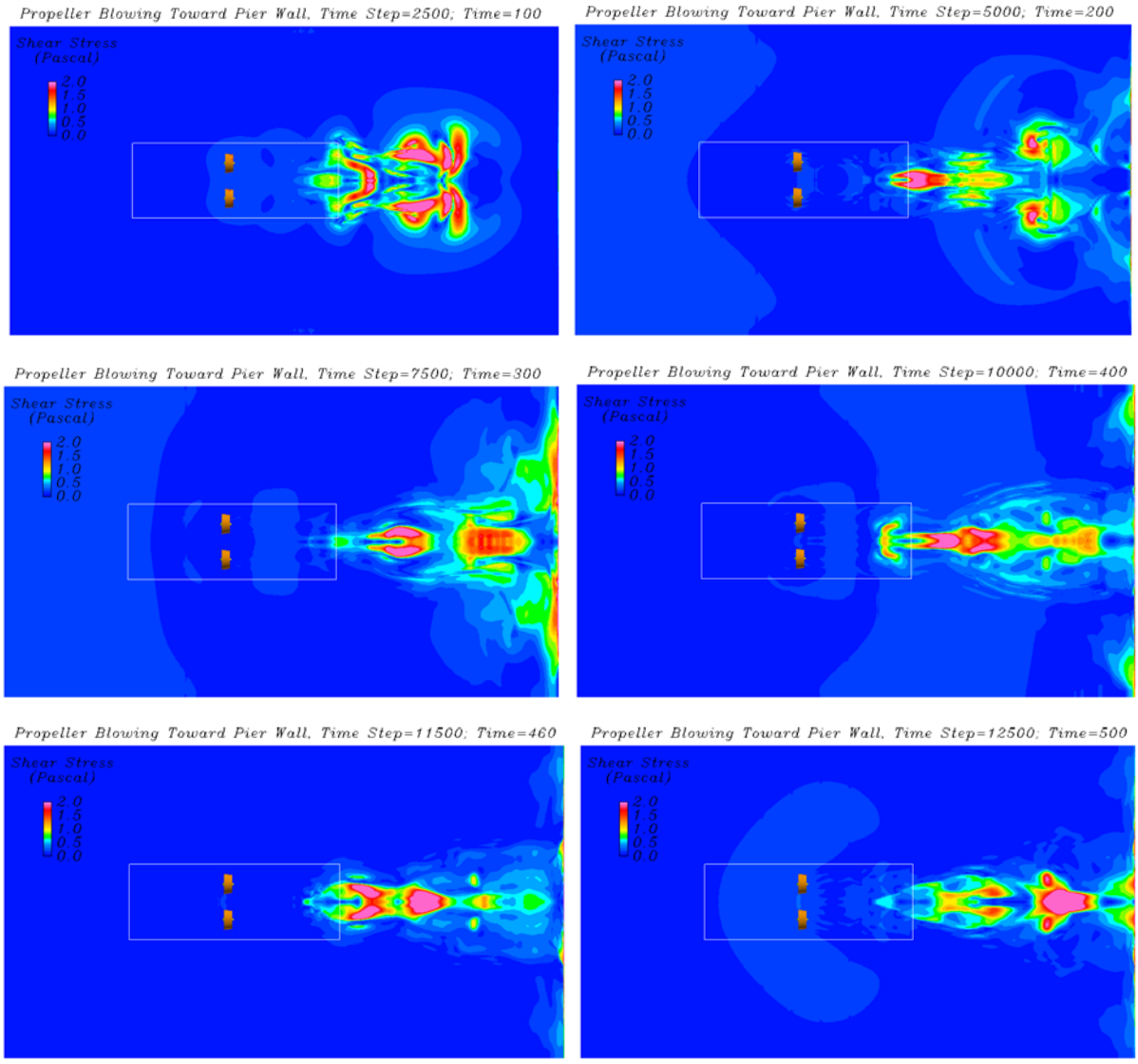

Figure 25. Shear Stress distribution on the seabed at $t/T_o = 100$, 200, 300, 400, 460, and 500; Case 2 with propeller blowing to pier wall.

Figure 26 shows the shear stress distributions on the sea bottom for Case 3 with propellers blowing parallel to a pier wall. Note that a different color bar scale was used in Figure 26 since the bottom shear stresses for Case 3 are several times higher than those observed in Cases 1 and 2. During the initial stage of simulation, a high shear stress region was developed around the tugboat stern region similar to those observed in Cases 1 and 2. As the propeller wake grew longer and wider, another high shear stress region was developed along the parallel pier wall, as shown in Figure 26(b)–(c).

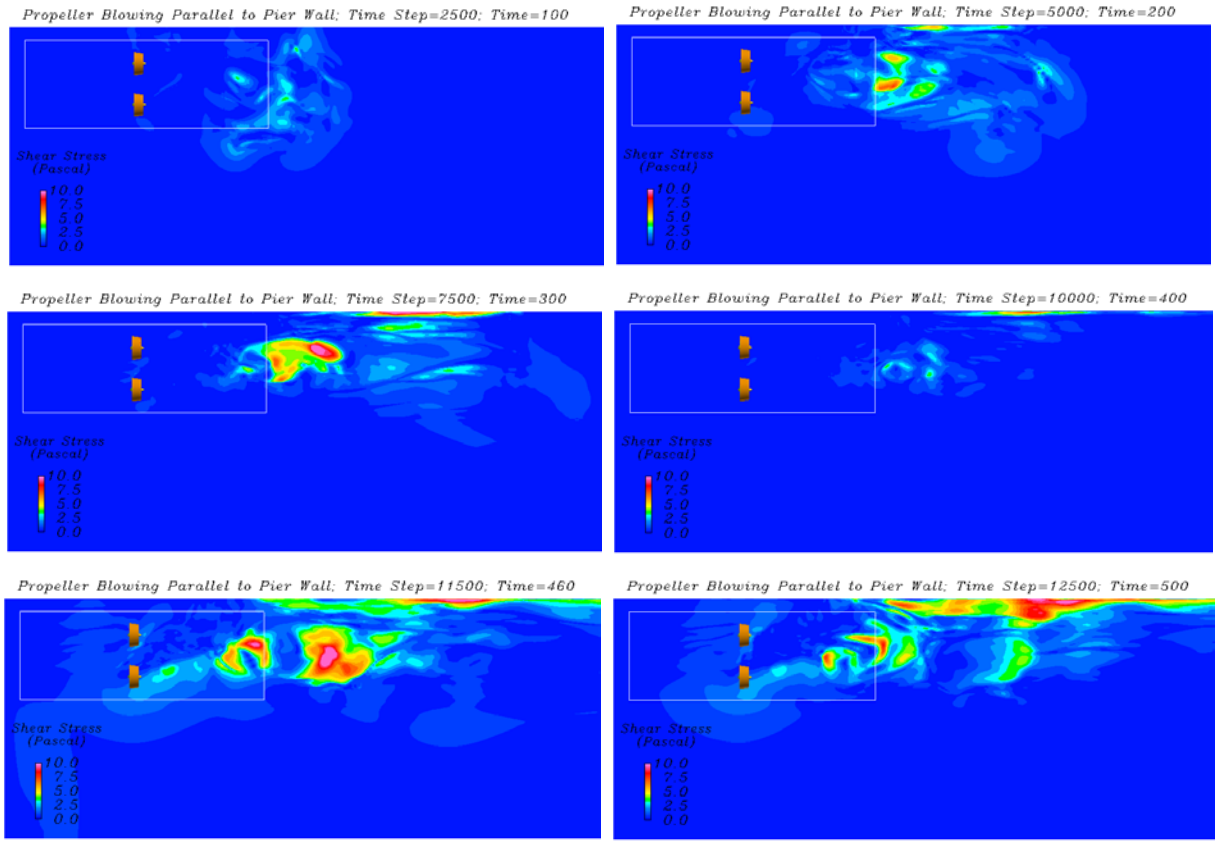

Figure 26. Shear Stress distribution on the seabed at t/T_o = 100, 200, 300, 400, 460, and 500; Case 3 with propeller blowing parallel to pier wall.

As shown earlier in Figures 19 through 23, a very strong interaction exists between the left and right propellers when the two right-handed propellers are rotating in the same direction. Consequently, the weaker left propeller wake (away from pier wall) was pushed closer to the sea bottom, while the stronger right propeller wake (near pier wall) was deflected slightly upward to the free surface. Note that the weaker left propeller wake actually produced considerably higher shear stresses in the near field because it is much closer to the sea bed than the stronger right propeller wake, as shown in Figure 22. In the far field, another high shear stress region exists adjacent to the parallel pier wall. A detailed examination of the propeller-induced flow field indicates that the second high shear stress region was produced by the stronger right propeller wake. At t/T_o = 500, the high shear stress regions is observed near the pier wall with a maximum shear stress of about 10.4 Pa at X/D = 16.3 behind the duct propellers.

A detailed comparison of the velocity and shear stress distributions for Cases 1 through 3 clearly illustrates that the sea bed shear stresses induced by the ducted propellers are strongly affected by the harbor configuration as well as the propeller rotating directions. Furthermore, as demonstrated in the

DDG 51 ship and P4876 propeller wash study, the shear stresses on the sea bottom also depend strongly on the water depth, ship geometry, underkeel clearance, ship speed, propeller type, and propeller operating conditions. To provide detailed shear stress distributions for different ships under site-specific harbor configurations, it is desirable to perform propeller wash study by solving the Navier–Stokes equations directly in conjunction with advanced turbulence models.

4. REFERENCES/BIBLIOGRAPHY

1. Briaud, J.-L. and H.C. Chen. 2006. "Levee Erosion by Overtopping During the Katrina Hurricane." *Proceedings of the Third International Conference on Scour and Erosion.* November 1–3, Amsterdam, The Netherlands.
2. Briaud, J.-L., H.-C Chen, Y. Li., and P. Nurtjahyo. 2004. "SRICOS-EFA Method for Complex Piers in Fine-Grained Soils," *ASCE Journal of Geotechnical and Geoenvironmental Engineering,* vol. 130, no. 11, pp. 1180–11191.
3. C.-J Chen, R. H. Bravo, H.-C. Chen, and Z. Xu. 1995. "Accurate Discretization of Incompressible Three-Dimensional Navier-Stokes Equations," *Numerical Heat Transfer, Part B: Fundamentals*, vol. 27, no. 4, pp. 371–392.
4. Chen C.-J. and H.-C. Chen. 1984. "Finite Analytic Numerical Method for Unsteady Two-dimensional Navier-Stokes Equations," *Journal of Computational Physics*, vol. 53, pp. 209–226.
5. Chen, C.-R. and H.-C. Chen. 2014. "CFD Simulation of Extreme Slamming on a Containership in Random Waves," *The 24th International Ocean and Polar Engineering Conference* (pp. 499–506). June 15–20, Busan, Korea.
6. Chen, H.-C. 2002. "Numerical Simulation of Scour Around Complex Piers in Cohesive Soil." *Proceedings of First International Conference on Scour of Foundations* (pp. 14–33). November 17–20, College Station, TX.
7. Chen, H.-C. 2009. "COSMIC – An Overset Grid Interpolation Method for Moving Body Applications." American Bureau of Shipping (ABS) Project Final Report. Texas A&M University, College Station, TX.
8. Chen, H.-C. 2010. "Time-Domain Simulation of Nonlinear Wave Impact Loads on Fixed Offshore Platform and Decks," *International Journal of Offshore and Polar Engineering*, vol. 20, no. 4, pp. 275–283.
9. Chen, H.-C. 2011. "CFD Simulation of Compressible Two-Phase Sloshing Flow in a LNG Tank," *International Journal of Ocean Systems Engineering,* vol. 1, no. 1, pp. 29–55.
10. Chen, H.-C. 2013. "CFD Simulation of Directional Short-Crested Waves on Jack-up Structure," *International Journal of Offshore and Polar Engineering*, vol. 23, no. 1, pp. 38–45.
11. Chen, H.-C., C.-R. Chen, and K. Huang. 2013. "CFD Simulation of Vortex-Induced and Wake-Induced Vibrations of Dual Vertical Risers." *Proceedings of 23rd International Offshore and Polar Engineering Conference* (ISOPE-I-13-457). June 30–July 5, Anchorage, AK.
12. Chen, H.-C. and M. Chen. 1998. "Chimera RANS Simulation of a Berthing DDG-51 Ship in Translational and Rotational Motions," *International Journal of Offshore and Polar Engineering*, vol. 8, no. 3, pp. 182–191.
13. Chen, H.-C. and S.-K. Lee. 2004. "Time-Domain Simulation of Four-Quadrant Propeller Flow by a Chimera Moving Grid Approach." *Civil Engineering in the Oceans VI Conference* (pp. 171–191). October 20–22, Baltimore, MD.
14. Chen, H.-C., W.-M. Lin, and Y.-W. Hwang. 2002a. "Turbulent Flow Induced by Multiple-Ship Operations in Confined Water," Paper No. EM-2002-123, 15th ASCE Engineering Mechanics Conference. June 2–5, Columbia University, New York, NY.
15. Chen, H.-C., W.-M. Lin, and Y.-W. Hwang. 2002b. "Validation and Application of Chimera RANS Method for Ship-Ship Interactions in Shallow Water and Restricted Waterway," 24th Symposium on Naval Hydrodynamics. July 8–13, Fukuoka, Japan.Chen, H.-C., W.-M. Lin,

D. A. Liut. and W.-Y. Hwang. 2003. “An Advanced Viscous Flow Computational Method for Ship-Ship Interactions in Shallow and Restricted Waterway,” International Conference on Marine Simulation and Ship Maneuverability (MARSIM’03). August 25–28, Kanazaawa, Japan.

17. Chen, H.-C., T. Liu, E. T. Huang, and D. A. Davis. 2000. “Chimera RANS Simulation of Ship and Fender Coupling for Berthing Operations,” *International Journal of Offshore and Polar Engineering*, vol. 10, no. 2, pp. 112–122.
18. Chen, H.-C. and E. T. Huang. 2003. “Time-Domain Simulation of Floating Pier and Multiple-Vessel Interactions by a Chimera RANS Method,” 7th International Symposium on Fluid Control, Measurement and Visualization. August 25–28, Sorrento, Italy.
19. Chen, H.-C. and V. C. Patel. 1988. “Near-Wall Turbulence Models for Complex Flows Including Separation,” *AIAA Journal*, vol. 26, no. 6, pp. 641–648.
20. Chen, H.-C., V.C. Patel, and S. Ju. 1990. “Solutions of Reynolds-Averaged Navier-Stokes Equations for Three-Dimensional Incompressible Flows,” *Journal of Computational Physics*, vol. 88, no. 2, pp. 305–336.
21. Chung, J. and G. M. Hulbert. 1993. “A Time Integration Algorithm for Structural Dynamics with Improved Numerical Dissipation: The Generalized-α Method,” *Journal of Applied Mechanics*, vol. 60, pp. 371–375.
22. Dettmer, W. and D. Peric. 2003. “An Analysis of the Time integration algorithms for the finite element solutions of incompressible Navier–Stokes Equations based on a Stabilised Formulation,” *Computer Methods in Applied Mechanics and Engineering*, vol. 192. pp. 1177–1226.
23. Huang, E.T. and H.-C. Chen. 2003. “Ship Berthing at a Floating Pier.” *Proceedings of 13th International Offshore and Polar Engineering Conference*, Volume III (pp. 683–690). May 25–30, Honolulu, HI.
24. Huang, E.T. and H.-C. Chen. 2007. “Influence of Site Specifics on Passing Ship Effects.” *Proceedings of 17th International Offshore and Polar Engineering Conference*, Volume III (pp. 2356–2363). July 1–6, Lisbon, Portugal.
25. Huang, E. T. and H.-C. Chen. 2010. “Passing Ship Effects at Typical Waterfronts,” *Proceedings of the ASCE PORTS 2010 Conference* (pp. 679688). April 25–28, Jacksonville, FL.
26. Huang, K., H.-C. Chen, and C.-R. Chen. 2010. “Vertical Riser VIV Simulation in Uniform Current,” *ASME Journal of Offshore Mechanics and Arctic Engineering*, vol. 132, no. 3, article no. 031101.
27. Huang, K., H.-C. Chen, and C.-R. Chen. 2011. “Numerical Scheme for Riser Motion Calculation during 3-D VIV Simulation,” *Journal of Fluids and Structures*, vol. 27, vo. 7, pp. 947–961.
28. Huang, K., H.-C. Chen, and C.-R. Chen. 2012. “Vertical Riser VIV Simulation in Sheared Current,” *International Journal of Offshore and Polar Engineering*, vol. 22, no. 2, pp. 142–149.
29. Chen, H.-C. and K. Yu. 2009. “CFD Simulation of Wave-Current-Body Interactions Including Greenwater and Wet Deck Slamming,” *Journal of Computers and Fluids*, vol. 38, no. 5, pp. 970–980.
30. Lee, S.-K. and H.-C. Chen. 2005. “The Influence of Propeller/Hull Interaction on Propeller Induced Cavitating Pressure.” *Proceedings of the 15th International Offshore and Polar Engineering Conference, Volume IV* (pp. 596–603). June 19–24, Seoul, Korea.

31. Pontaza, J. P., H.-C. Chen, and S.-K. Lee. 2006. “Numerical Simulation of Coupled Ship and Propeller Flows.” *Proceedings of 16th International Offshore and Polar Engineering Conference, Volume IV* (pp. 468–474), May 28–June 2, San Francisco, CA.
32. Pontaza J. P., H.-C. Chen, and J. N. Reddy. 2005, “A Local-analytic-based Discretization Procedure for the Numerical Solution of Incompressible Flows.” *International Journal for Numerical Methods in Fluids*, vol. 49, no. 6, pp. 657–699.

REPORT DOCUMENTATION PAGE

Form Approved
OMB No. 0704-01-0188

PLEASE DO NOT RETURN YOUR FORM TO THE ABOVE ADDRESS.

1. REPORT DATE *(DD-MM-YYYY)*	**2. REPORT TYPE**	**3. DATES COVERED** *(From - To)*
August 2016	Final	R

4. TITLE AND SUBTITLE

FANS Simulation of Propeller Wash at Navy Harbors (ESTEP Project ER-201031)

5a. CONTRACT NUMBER

5b. GRANT NUMBER

5c. PROGRAM ELEMENT NUMBER

6. AUTHORS

Pei-Fang Wang
SSC Pacific

Hamn-Ching Chen
Texas A&M University

5d. PROJECT NUMBER

5e. TASK NUMBER

5f. WORK UNIT NUMBER

7. PERFORMING ORGANIZATION NAME(S) AND ADDRESS(ES)

SSC Pacific
53560 Hull Street
San Diego, CA 92152–5001

8. PERFORMING ORGANIZATION REPORT NUMBER

TR 2085

9. SPONSORING/MONITORING AGENCY NAME(S) AND ADDRESS(ES)

Environmental Security Technology Certification Program (ESTCP)
4800 Mark Center Drive, Suite 17D08
Alexandria, VA 22350-3605

10. SPONSOR/MONITOR'S ACRONYM(S)

11. SPONSOR/MONITOR'S REPORT NUMBER(S)

12. DISTRIBUTION/AVAILABILITY STATEMENT

Approved for public release.

13. SUPPLEMENTARY NOTES

14. ABSTRACT

Propeller wash induces high shear stresses on seafloor which may cause sediment resuspension in Department of Defense (DoD) harbors. To improve understanding of the sediment erosion, transport, dispersion, and re-deposition processes, it is desirable that advanced computational fluid dynamics models should be used to provide detailed resolution of the velocities and bottom shear stresses induced by the propeller wash in confined shallow water basins. In this study, the Finite-Analytic Navier–Stokes code was employed to solve the Reynolds-Averaged Navier–Stokes equations in conjunction with advanced near-wall turbulence model for several propeller-wash scenarios involving an Arleigh Burke-class destroyer with twin-screw propellers and a tugboat with two ducted propellers. This model enables us to evaluate the effect of water depth, ship speed, propeller rotating speed, and pier wall configuration on the propeller-induced shear stresses distributions.

15. SUBJECT TERMS

Mission Area: Environmental Science
FANS-3D code; Reynolds-Averaged Naier–Stokes equations; finite analytic base discretion; DDG 51 ship;
FANS model simulation scenarios; tugboat with ducted propellers; estimated bottom shear stress

16. SECURITY CLASSIFICATION OF:			**17. LIMITATION OF ABSTRACT**	**18. NUMBER OF PAGES**	**19a. NAME OF RESPONSIBLE PERSON**
a. REPORT	**b. ABSTRACT**	**c. THIS PAGE**			Pei-Fang Wang
U	U	U	U	87	**19B. TELEPHONE NUMBER** *(Include area code)* (619) 553-2768

INITIAL DISTRIBUTION

84300	Library	(1)
85300	Archives	(1)
71750	P.F. Wang	(1)

Defense Technical Information Center
Fort Belvoir, VA 22060–6218 (1)

Hamm-Ching Chen
Ocean Engineering Program
Zachry Department of Civil Engineering
Texas A&M University
College Station, TX 77843-3136 (1)

Approved for public release.

SSC Pacific
San Diego, CA 92152-5001